



An ALMA Survey of Submillimeter Galaxies in the Extended *Chandra* Deep Field South: Spectroscopic Redshifts

A. L. R. Danielson¹, A. M. Swinbank^{1,2}, Ian Smail^{1,2}, J. M. Simpson¹, C. M. Casey^{3,4}, S. C. Chapman⁵, E. da Cunha⁶, J. A. Hodge⁷, F. Walter⁸, J. L. Wardlow¹, D. M. Alexander¹, W. N. Brandt⁹, C. de Breuck¹⁰, K. E. K. Coppin¹¹, H. Dannerbauer¹², M. Dickinson¹³, A. C. Edge¹, E. Gawiser¹⁴, R. J. Ivison¹⁰, A. Karim¹⁵, A. Kovacs¹⁶, D. Lutz¹⁷, K. Menten¹⁵, E. Schinnerer⁷, A. Weiß¹⁵, and P. van der Werf⁷

¹ Centre for Extragalactic Astronomy, Durham University, Department of Physics, South Road, Durham DH1 3LE, UK; a.m.swinbank@durham.ac.uk

² Institute for Computational Cosmology, Durham University, South Road, Durham DH1 3LE, UK

³ Department of Astronomy, The University of Texas at Austin, 2515 Speedway Boulevard Stop C1400, Austin, TX 78712, USA

⁴ Department of Physics and Astronomy, University of California, Irvine, Irvine, CA 92697, USA

⁵ Department of Physics and Atmospheric Science, Dalhousie University, Halifax, NS B3H 4R2, Canada

⁶ Research School of Astronomy and Astrophysics, Australian National University, Canberra, ACT 2611, Australia

⁷ Leiden Observatory, Leiden University, P.O. Box 9513, 2300 RA Leiden, The Netherlands

⁸ Max-Planck-Institut für Astronomie, Königstuhl 17, D-69117 Heidelberg, Germany

⁹ Department of Astronomy and Astrophysics and the Institute for Gravitation and the Cosmos, The Pennsylvania State University, State College, PA 16801, USA

¹⁰ European Southern Observatory, Karl Schwarzschild Straße 2, D-85748, Garching, Germany

¹¹ Centre for Astrophysics Research, Science and Technology Research Institute, University of Hertfordshire, College Lane, Hatfield AL10 9AB, UK

¹² Universität Wien, Institut für Astrophysik, Türkenschanzstraße 17, A-1180, Wien, Austria

¹³ National Optical Astronomy Observatory, Tucson, AZ 85719, USA

¹⁴ Department of Physics and Astronomy, Rutgers University, Piscataway, NJ 08854, USA

¹⁵ Max-Planck-Institut für Radioastronomie, Auf dem Hügel 69, D-53121 Bonn, Germany

¹⁶ Astronomy Department, University of Minnesota, MN 12345, USA

¹⁷ Max-Planck-Institut für extraterrestrische Physik, Giessenbachstraße, D-85748, Garching, Germany

Received 2016 August 24; revised 2017 March 16; accepted 2017 March 22; published 2017 May 9

Abstract

We present spectroscopic redshifts of $S_{870\ \mu\text{m}} \gtrsim 2$ mJy submillimeter galaxies (SMGs), which have been identified from the ALMA follow-up observations of 870 μm detected sources in the Extended *Chandra* Deep Field South (the ALMA-LESS survey). We derive spectroscopic redshifts for 52 SMGs, with a median of $z = 2.4 \pm 0.1$. However, the distribution features a high-redshift tail, with $\sim 23\%$ of the SMGs at $z \geq 3$. Spectral diagnostics suggest that the SMGs are young starbursts, and the velocity offsets between the nebular emission and UV ISM absorption lines suggest that many are driving winds, with velocity offsets of up to $2000\ \text{km s}^{-1}$. Using the spectroscopic redshifts and the extensive UV-to-radio photometry in this field, we produce optimized spectral energy distributions (SEDs) using MAGPHYS, and use the SEDs to infer a median stellar mass of $M_* = (6 \pm 1) \times 10^{10} M_\odot$ for our SMGs with spectroscopic redshift. By combining these stellar masses with the star formation rates (measured from the far-infrared SEDs), we show that SMGs (on average) lie a factor of ~ 5 above the so-called “main sequence” at $z \sim 2$. We provide this library of 52 template fits with robust and uniquely well-sampled SEDs as a resource for future studies of SMGs, and also release the spectroscopic catalog of ~ 2000 (mostly infrared-selected) galaxies targeted as part of the spectroscopic campaign.

Key words: galaxies: evolution – galaxies: formation – galaxies: high redshift – galaxies: starburst

Supporting material: machine-readable tables

1. Introduction

Submillimeter galaxies (SMGs) with $850\ \mu\text{m}$ fluxes of $S_{850} > 1$ mJy represent a population of dusty starbursts whose space density peaked ~ 10 Gyr ago. Although they are relatively rare, their far-infrared luminosities ($L_{\text{IR}} > 2 \times 10^{12} L_\odot$) imply that high star formation rates ($\gtrsim 300 M_\odot\ \text{yr}^{-1}$), and thus SMGs, appear to contribute at least 20% of the total cosmic star formation rate density over $z = 1\text{--}4$ (e.g., Chapman et al. 2005; Barger et al. 2012; Casey et al. 2014; Swinbank et al. 2014). If they can maintain their star formation rates, SMGs also have the potential to consume all of their cold gas reservoir within just 100 Myr (e.g., Tacconi et al. 2008; Bothwell et al. 2013), and thus they double their stellar masses within their short but intense lifetime (e.g., Hainline et al. 2009; Magnelli et al. 2012). Their ability to form up to $10^{11} M_\odot$ of stars within a short period of time makes SMGs candidates of progenitors of $z = 1\text{--}2$ compact quiescent galaxies (Toft et al. 2014; Ikarashi et al. 2015;

Simpson et al. 2015a) as well as local massive ellipticals (e.g., Lilly et al. 1999; Genzel et al. 2003; Simpson et al. 2014). These characteristics suggest that bright SMGs represent an essential population for models of galaxy formation and evolution (e.g., Efstathiou & Rowan-Robinson 2003; Baugh et al. 2005; Swinbank et al. 2008; Narayanan et al. 2009; Davé et al. 2010; Hayward et al. 2011; Lacey et al. 2016).

However, to identify the physical processes that trigger the starbursts, measure the internal dynamics of the cold (molecular) and ionized gas, and infer stellar masses first requires accurate redshifts. To date, the largest such spectroscopic survey of 870 μm selected submillimeter sources was carried out by Chapman et al. (2005) who targeted a sample of 104 radio-identified, SCUBA-detected submillimeter sources spread across seven extragalactic survey fields. Using rest-frame UV spectroscopy with the Low-resolution Imaging Spectrograph (LRIS) on the Keck telescope, they derived spectroscopic redshifts for 73 submillimeter sources with a

median redshift of $z \sim 2.4$ for the radio-selected sample (with a maximum redshift in their sample of $z = 3.6$).

Although the requirement for a radio detection in these previous surveys was a necessary step to identify the most probable galaxy counterpart responsible for the submillimeter emission, the radio wavelengths do not benefit from the same negative K-correction as longer submillimeter wavelengths and indeed, above $z \sim 3.5$, the 1.4 GHz flux of a galaxy with a star formation rate of $\sim 100 M_{\odot} \text{ yr}^{-1}$ falls below $\sim 15 \mu\text{Jy}$ and thus below the typical sensitivity limit of deep radio surveys. This has the potential to bias the redshift distribution to $z \lesssim 3.5$, especially if a significant fraction of submillimeter sources do not have multi-wavelength counterparts. Indeed, in single-dish 850 μm surveys, up to 50% of all submillimeter sources are undetected at radio wavelengths (e.g., Ivison et al. 2005, 2007; Biggs et al. 2011). Some progress can be made by targeting lensed sources whose multi-wavelength identifications are less ambiguous, and indeed spectroscopic redshifts have been derived for SMGs up to $z \sim 5$ (e.g., Weiß et al. 2013).

Due to the angular resolution and sensitivity of the ALMA interferometer, it has become possible to identify the counterparts of submillimeter sources to $\lesssim 0''.3$ accuracy without recourse to statistical associations at other wavelengths. To identify a sample of SMGs in a well studied field with a well defined selection function, Hodge et al. (2013) undertook an ALMA survey of 122 SMGs found in the Extended *Chandra* Deep Field South (ECDFS): the ‘‘ALESS’’ survey. This survey followed up 122 of the 126 submillimeter sources originally detected with the LABOCA instrument on the Atacama Pathfinder Experiment 12 meter telescope (APEX); the LABOCA ECDFS Sub-mm Survey (LESS; Weiß et al. 2009). Each LESS submillimeter source was targeted with ALMA at 870 μm (Band 7). The typical FWHM of the ALMA synthesized beam was $\sim 1''.5$ (significantly smaller than the LABOCA $19''.2$ beam), thus allowing us to directly pinpoint the position of the SMG precisely.

From these data, Karim et al. (2013; see also Simpson et al. 2015b) showed that statistical identifications (e.g., using radio counterparts) were incorrect in $\sim 30\%$ of cases, while the single-dish submillimeter sources also suffer from significant ‘‘multiplicity,’’ with $>35\%$ of the single-dish sources resolved into multiple SMGs brighter than $\gtrsim 1 \text{ mJy}$. This flux limit corresponds approximately to a far-infrared luminosity of $L_{\text{FIR}} \gtrsim 10^{12} L_{\odot}$ at $z \sim 2$, and so it appears that a large fraction of the single-dish submillimeter sources often contain two (or more) Ultra-Luminous Infrared Galaxies (ULIRGs). Consequently, a new ALESS SMG catalog was defined comprising 131 SMGs (Hodge et al. 2013).

One of the primary goals of the ALESS survey is to provide an unbiased catalog of SMGs for which we can derive molecular gas masses, as well as measure spatially resolved dynamics of the gas and stars in order to identify the triggering mechanisms that cause the burst of star formation. The first necessary step in this process is to derive the precise spectroscopic redshifts. To this end, we have undertaken a spectroscopic survey of ALMA-identified SMGs using VLT, Keck, and Gemini (supplemented by ALMA) and, in this paper, we describe the UV, optical, and near-infrared spectroscopic follow-up. We use the resulting redshifts to investigate the redshift distribution, the environments and typical spectral features of these SMGs. In addition, we use these precise redshifts to better constrain the SED fitting from UV-to-radio

wavelengths and provide template SEDs for the ALESS SMG population.

The structure of the paper is as follows. We discuss the observations and the data reduction in Section 2, followed by redshift identification and sample properties in Section 3. In Section 4, we show the ALESS redshift distribution and discuss the spectroscopic completeness. In Section 5, we discuss the velocity offsets of various different spectral lines, search for evidence of stellar winds and galaxy-scale outflows, and investigate the environments of SMGs and the individual and composite spectral properties. We present our conclusions in Section 6. In the Appendices, we give the table of ALESS SMG redshifts and provide information on individual SMGs from the sample.

Unless otherwise stated, the quoted errors on the median values within this work are determined through bootstrap analysis and are quoted as the equivalent of 68.3% confidence limits. Throughout the paper, we use a Λ CDM cosmology with $H_0 = 72 \text{ km s}^{-1} \text{ Mpc}^{-1}$, $\Omega_m = 0.27$, and $\Omega_{\Lambda} = 1 - \Omega_m$ (Spergel et al. 2003) and a Chabrier initial mass function (IMF; Chabrier 2003). Unless otherwise noted, all magnitudes are on the AB system.

2. Observations and Reduction

2.1. Sample Definition

The 870 μm LESS survey (Weiß et al. 2009) was undertaken using the LABOCA camera on APEX, covering an area of 0.5×0.5 centered on the ECDFS. The total exposure time for the survey was 310 hr, reaching a 1σ sensitivity of $\sigma_{870 \mu\text{m}} \sim 1.2 \text{ mJy beam}^{-1}$ with a beam of $19''.2$ FWHM. In total, we identified 126 submillimeter sources above a signal-to-noise of 3.7σ . Follow-up observations of the LESS sources were carried out with ALMA (the ALMA-LESS, ALESS program). Details of the ALMA observations are described in Hodge et al. (2013) but in summary, the 120 s observations for each source were taken between 2011 October and November in the Cycle 0 Project #2011.1.00294.S. These submillimeter interferometric identifications confirmed some of the probabilistically determined counterparts (Biggs et al. 2011; Wardlow et al. 2011) but also revealed some misidentified counterparts and a significant number of new counterparts. Therefore, the ALESS SMG catalog was formed, comprising a main (hereafter MAIN) catalog of 99 of the most reliable ALMA-identified SMGs (i.e., lying within the the primary beam FWHM of the best-quality maps). A supplementary (hereafter SUPP) catalog was also defined comprising 32 ALMA-identified SMGs extracted from outside the ALMA primary beam, or in lower quality maps (Hodge et al. 2013). When searching for spectroscopic redshifts, we included both the MAIN and SUPP sources, and in Section 4 we demonstrate that the inclusion of SUPP sources makes very little quantitative difference to the statistics of the redshift distribution.

To search for spectroscopic redshifts, we initiated an observing campaign using the the FOcal Reducer and low Dispersion Spectrograph (FORSD) and Visible MultiObject Spectrograph (VIMOS) on VLT, but to supplement these observations, and in particular to increase the wavelength coverage and probability of determining redshifts, we also obtained observations with XSHOOTER on VLT, the Gemini Near-Infrared Spectrograph (GNIRS) and the Multi-Object Spectrometer for Infra-Red Exploration (MOSFIRE) on the

Table 1
Spectroscopic Redshifts for the Full Sample

ID	R.A. (J2000)	Decl. (J2000)	z_{spec}	Q	Inst	ID	R.A. (J2000)	Decl. (J2000)	z_{spec}	Q	Inst
101	53.30820	-27.93445	4.6892	1	F	104	53.26036	-27.94606	1.9469	3	VF
106	52.90094	-27.91398	2.3484	3	VMF	107	52.89957	-27.91209	...	4	VMF
108	52.89780	-27.90952	...	4	VF	109	52.90089	-27.91278	3.0159	2	V
110	52.87580	-27.98573	1.4135	1	F	112	52.87865	-27.98229	0.4342	1	F
113	53.23814	-28.01708	1.3648	3	VF	114	53.23651	-28.01645	...	4	VF
116	53.31593	-27.76045	0.7516	1	VF	117	53.02072	-27.51948	0.9610	2	VF
118	53.01840	-27.52046	0.7283	3	VF	119	53.04730	-27.87038	...	4	F
280	53.08039	-27.87200	...	3	V	122	53.19980	-27.90448	3.1977	3	V
123	53.20365	-27.71445	...	4	VF	123b	53.20339	-27.71603	2.8382	2	V
124	52.96913	-28.05492	...	4	V	127	53.07793	-27.62877	...	4	V

Notes. The labels in the instrument column are defined as F = VLT/FORS2, V = VLT/VIMOS, X = VLT/XSHOOTER, M = Keck/MOSFIRE (Band *H* or *K*), D = Keck/DEIMOS, G = Gemini/GNIRS. The quality flag (Q) for the spectroscopic redshifts is $Q = 1$ for secure redshifts; $Q = 2$ for redshifts measured from only one or two strong lines; $Q = 3$ for tentative redshifts measured based on one or two very faint features; $Q = 4$ for those sources that were targeted but no redshift could be determined.

(This table is available in its entirety in machine-readable form.)

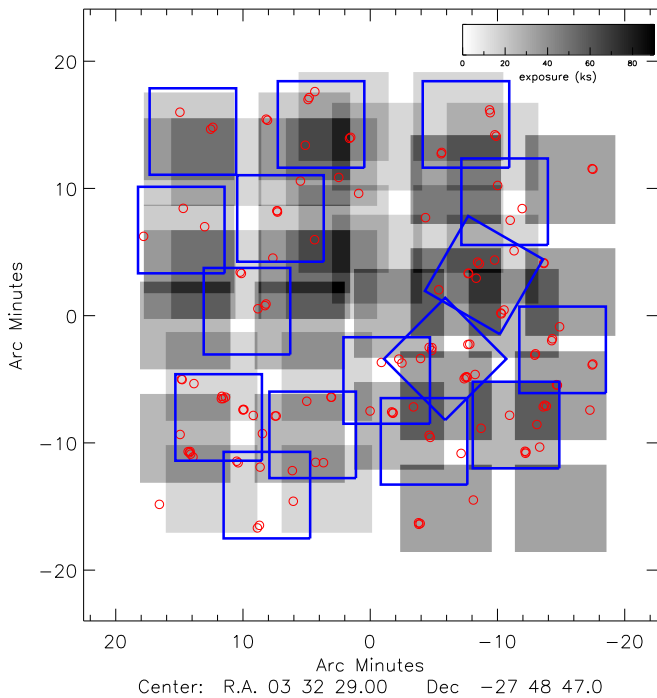


Figure 1. Coverage of our 10 VIMOS pointings (grayscale) and 16 FORS2 pointings (blue boxes) in the EDFS. The ALESS SMG positions are shown as small red circles. VIMOS has four quadrants separated by small gaps. There is significant overlap between the VIMOS pointings, we therefore show the pointings here with the darkest areas corresponding to the regions with the longest total exposure time. Our FORS2/VIMOS program covers 62 out of the 109 targeted SMGs in the EDFS.

Keck I telescope, all of which cover the near-infrared. As part of a spectroscopic campaign targeting *Herschel*-selected galaxies in the EDFS, ALESS SMGs were included on DEEP Imaging Multi-Object Spectrograph (DEIMOS) slit masks on Keck II (e.g., Casey et al. 2012). These observations probe a similar wavelength range to FORS2 targeting some of the ALMA-identified SMGs that could not be targeted with VLT (due to slit collisions). In total, we observed 109 out of the 131 ALESS SMGs in the combined MAIN and SUPP samples. In many cases we have ALESS SMGs with spectra from five

different spectrographs covering a broad wavelength range and we can cross-check the spectroscopic redshifts across all of the instruments. Next, we discuss the various instruments involved in our survey. We note that for all observations described below, flux calibration was carried out using standard stars to calibrate the instrumental response.

2.2. VLT FORS2/VIMOS

Our spectroscopic program aimed to target as many of the ALESS SMGs as possible using a dual approach with FORS2 and VIMOS (for a typical SMG redshift of $z \sim 1-3$, we are sensitive to Ly α and UV ISM lines with VIMOS or [O II] $\lambda 3727$ with FORS2). In total, we observed for 100 hr each with VIMOS and FORS as part of program 183.A-0666. We used deep exposures on 10 (overlapping) VIMOS masks to cover the field, plus deep integrations for 16 FORS masks (which cover a subset of the field but target the regions with the highest density of ALMA SMGs; Figure 1). All of the FORS observations were carried out in gray time and all of the VIMOS observations were carried out in dark time during service mode runs with seeing $\leq 0''.8$ and clear sky conditions (transparency variations below 10%). Our dual-instrument approach allowed us to probe a large wavelength range using VIMOS LR-Blue grism (4000–6700 Å) and FORS2 300I (6000–11000 Å). When designing the slit masks, the first priority was always given to the SMGs, but we also in-filled the masks with other mid- or far-infrared-selected galaxies from the FIDEL *Spitzer* survey (Magnelli et al. 2009), the HerMES and PEP *Herschel* surveys of this field (Lutz et al. 2011; Oliver et al. 2012), $S_{1.4 \text{ GHz}} > 30 \mu\text{Jy}$ radio sources and *Chandra* X-ray sources (Lehmer et al. 2005; Luo et al. 2008) or optical/near-infrared color selected galaxies (see Table 1 and Figure 15).

In Figure 1, we show the spectroscopic coverage of the EDFS from our FORS2 and VIMOS programs, where the darkest areas demonstrate the areas with the longest total exposure time and the FORS2 pointings are overlaid. In total, we recorded 5221 galaxy spectra, targeting 2454 (unique) galaxies.

2.2.1. FORS2

FORS2 covers the the wavelength range $\lambda = 3300-11000 \text{ Å}$ and provides an image scale of $0''.25 \text{ pix}^{-1}$ in the standard readout

mode (2×2 binning). FORS2 was used in its multi-object spectroscopy mode with exchangeable masks (MXU). We varied the slit length and orientation for each target in order to observe the maximum number of sources on each mask (Figure 1), but we consistently used a slit width of $1''$. We used ~ 40 – 70 slits per mask and the OG590 order-sorting filter with the 300I grism, which results in a wavelength range covering 6000 – 11000 Å. The typical resolution in this configuration is $R = \lambda/\Delta\lambda \sim 660$. We used 16 pointings, though in a small number of cases, we moved slits between exposures if there were multiple sources within $\sim 5''$ which could not be simultaneously observed on a mask. Each mask was observed in blocks of 3×900 s with each exposure nodded up and down the slits by $\sim 1''$ to aid sky-subtraction and cosmic-ray removal when the images were combined. Each mask was typically observed six times (with a range of three to nine times depending on the number of SMGs on the mask and their median brightness), resulting in an on-source exposure time of 4.5 hr (with a range of 2.25–6.75 hr).

We reduced the data using the spectroscopic reduction package from Kelson (2003) adapted for use with FORS2 data FORS2 pipeline. The pipeline produces two-dimensional, bias-corrected, flat-fielded, wavelength-calibrated, sky-subtracted images. Individual exposures were combined in two dimensions by taking a median of the frames and sigma clipping. We then extracted one-dimensional spectra over the full spatial-extent of the continuum/emission lines visible, or in the case where no emission was obvious in the two-dimensional image, we extracted data from the region around the expected source position.

2.2.2. VIMOS

The VIMOS observations were undertaken in multi-object spectroscopy (MOS) mode. VIMOS consists of four quadrants each of a field of view of $7' \times 8'$ with a detector pixel scale of $0''.205 \text{ pix}^{-1}$. Each observing block comprised 3×1200 s exposures dithering $\pm 1''$ along the slit. The exposure time per mask was 3–9 hr, again depending on the number of SMGs on the mask and their average brightness. Slit widths of $1''$ were used, for which the typical resolution is $R \sim 180$ and the dispersion is 5.3 Å pix^{-1} for the LR_blue grism with the OS_blue order-sorting filter (~ 4000 – 6700 Å). We used 40–160 slits per quadrant, totalling 160–400 slits over the four quadrants. The data were reduced using the standard ESOREX pipeline package for VIMOS. The frames were stacked in two dimensions before extracting the one-dimensional spectra. In a number of cases, the data suffer from overlapping spectra, which results in a second-order overlapping the adjacent spectrum (this can be seen in the VIMOS two-dimensional spectrum of ALESS 057.1 in Figure 2).

2.3. XSHOOTER

To improve the wavelength coverage of our observations, we also obtained XSHOOTER observations of 20 ALESS SMGs. XSHOOTER simultaneously observes from UV to near-infrared wavelengths covering wavelength ranges of 3000 – 5600 Å, 5500 – 10200 Å, and 10200 – 24800 Å for the UV (UVB), visible (VIS), and near-infrared (NIR) arms respectively. Targets were prioritized for XSHOOTER follow-up based on their K -band magnitudes. Our XSHOOTER observations were taken in visitor mode as part of program 090.A-0927(A) from 2012 December 7–10 in dark time.

We observed each source for ~ 1 hr in generally clear conditions with a typical seeing of $\sim 1''$. Our observing strategy was 4×600 s exposures per source, nodding the source up and down the slit. The pixel scales were $0''.16$, $0''.16$, and $0''.21 \text{ pix}^{-1}$ for the UVB, VIS, and NIR arms respectively. The slits were all $11''$ long and $0''.9$ wide for the VIS and NIR arms and $1''$ wide for the UVB arm. The typical resolution was $R \sim 4350$, 7450 , 5300 for the UVB, VIS, and NIR arms respectively. The data reduction was carried out using the standard ESOREX pipeline package for XSHOOTER.

2.4. MOSFIRE

We also targeted 36 ALESS SMGs with the MOSFIRE spectrograph on Keck I (2012B_H251M, 2013B_U039M, and 2013B_N114M) in H - (1.46 – $1.81 \mu\text{m}$) and K -band (1.93 – $2.45 \mu\text{m}$). Observations were taken in clear or photometric conditions with the seeing varying from $0''.4$ to $0''.9$. In all cases, we used slits of width $0''.7$. The pixel scale of MOSFIRE is $0''.18 \text{ pix}^{-1}$ and the typical spectral resolution for this slit width is $R \sim 3270$. The total exposure time per mask was 2.2–3.6 ks, which was split into 120 s (H -band) and 180 s (K -band) exposures, with an ABBA sequence and a $1''.5$ nod along the slit between exposures. Data reduction was completed with MOSPY.

2.5. DEIMOS

We targeted 71 of the ALESS SMGs as “mask infill” during a Keck II DEIMOS spectroscopy program to measure redshifts for *Herschel*/SPIRE sources (program 2012B_H251). The data were taken on 2012 December 9–10 in clear conditions with seeing between $1''$ and $1''.3$. We used a setup with the 600ZD ($600 \text{ lines mm}^{-1}$) grating with a 7200 Å blaze angle and the GG455 blocking filter, which resulted in a wavelength range of 4850 – 9550 Å. Slit widths of $0''.75$ were used and the masks were filled with 40–70 slits per mask. The pixel scale of DEIMOS is $0''.1185 \text{ pix}^{-1}$ and the typical resolution was $R \sim 3000$. Individual exposures were 1200 s, and the total integration times were 2–3 hr. The data were reduced using the DEEP2 DEIMOS data reduction pipeline (Cooper et al. 2012; Newman et al. 2013).

2.6. GNIRS

GNIRS was used to target eight ALESS SMGs as (program GN-2012B-Q-90) between 2012 November 10–15 and December 4–23. The targets were selected based on their K -band magnitude and whether they had a photometric redshift that was predicted to place strong emission lines in the near-infrared. The instrument was used in cross-dispersing mode (via the SXD prism with 32 lines mm^{-1}), using the short camera, with slit widths of $0''.3$, slit lengths of $7''$ and a pixel scale of $0''.15 \text{ pix}^{-1}$. The wavelength coverage with this setup is 9000 – 25600 Å, typically with $R \sim 1700$. Our observing strategy comprised 200 s exposures and nodding up and down the slit by $\sim 1''$. Each observing block comprised eight coadds of three exposures, resulting in an exposure of ~ 1.3 hr per source. The GNIRS data were reduced using the Gemini IRAF package.

2.7. ALMA

Spectroscopic redshifts for two of our SMGs, ALESS 61.1 and ALESS 65.1, were determined from serendipitous detections

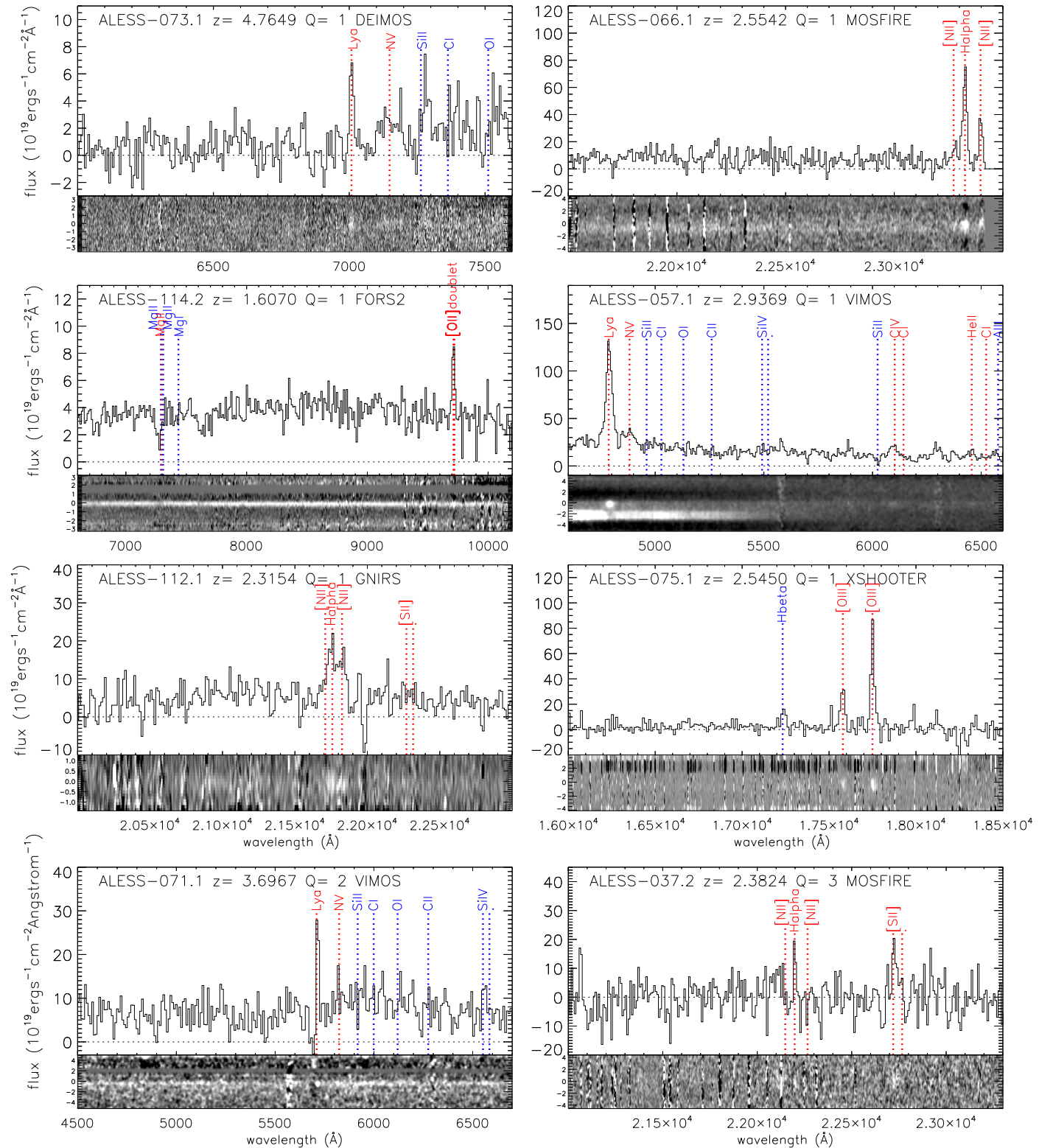


Figure 2. Example one- and two-dimensional spectra of ALESS SMGs from each spectrograph used. The upper three rows are high quality ($Q = 1$) spectra, while the bottom row shows lower quality examples ($Q = 2$ and 3 spectra) and we mark identified and potential features in all panels, where red dashed lines mark typical emission lines and blue dashed lines mark typical absorption lines. In ALESS 057.1 (an X-ray AGN), the bright continuum below the central strong emission line and continuum is contamination from higher order emission from an adjacent slit on the VIMOS mask. ALESS 037.2 is an example of a $Q = 3$ redshift where the redshift is determined from narrow $H\alpha$, though the apparent ratio of $S\ II/H\alpha$ is unusually high.

of the $[C\ II]\lambda 158\ \mu\text{m}$ line in the ALMA band (Swinbank et al. 2012). Although based on single line identifications, both redshifts have been confirmed by the identification of $^{12}\text{CO}(1-0)$ emission using ATCA (Huynh et al. 2013, 2017).

Once all of the data were collected from the different spectrographs, we collated the spectra for each ALESS SMG. The instruments used to observe each SMG are listed in Table 2.

3. Analysis

3.1. Redshift Identification

To determine redshifts for the sample, the one- and two-dimensional spectra (for all ~ 2000 galaxies) were independently examined by two investigators (AMS and ALRD). Any emission/absorption features that were identified were fit with Gaussian profiles to determine their central wavelengths. In the FORS2, VIMOS, and DEIMOS data, the most commonly identified lines were Ly α , C IV $\lambda\lambda 1548.89, 1550.77$ Å, C III $\lambda 1909$ Å, He II $\lambda 1640$ Å and [O II] $\lambda\lambda 3726.03, 3728.82$ Å. In the near-infrared, we typically detect H α , N II $\lambda 6583$ and [O III] $\lambda\lambda 4959, 5007$ and in a small number of cases, H β (see Tables 2 and 3). The optical/near-infrared counterparts of the SMGs are often faint and we detect continuum in only $\sim 50\%$ of the 52 SMGs for which we determine a redshift, (compared to $\sim 75\%$ for the radio-identified submillimeter sources in Chapman et al. 2005).

The spectra often only contain weak continuum, emission, and/or absorption lines, making redshifts difficult to determine robustly. We therefore assign four quality flags to our spectroscopic data.

1. $Q = 1$ denotes a secure redshift where multiple features were identified from bright emission/absorption lines;
2. $Q = 2$ denotes a redshift but derived from one or two bright emission (or strong absorption) lines;
3. $Q = 3$ is a tentative redshift based on one (or sometimes two tentative) emission or absorption lines. In these cases, we often use the photometric redshift as a guide to identify the line. These redshifts are therefore not independent of the photometric redshifts and are thus highlighted in the analysis; and
4. $Q = 4$ is assigned to galaxies with no emission lines or continuum detected and so no redshift could be determined.

Examples of spectra from which $Q = 1-3$ redshifts are determined are shown in Figure 2. Since the EDFS has been the focus of extensive spectroscopic campaigns (though focusing mainly on bright optical/UV-selected galaxies) six of our ALMA SMGs have published archival spectroscopic redshifts, and we highlight these in Table 2.¹⁸

The emission/absorption lines we are using to derive redshifts have a range of physical origins within the galaxies. For example, nebular emission lines arise from H II regions and thus are expected to trace the systemic redshift, whereas UV ISM lines can trace outflowing material and thus can be offset from the systemic redshift by several 100 km s^{-1} (e.g., Erb et al. 2006; Steidel et al. 2010). Ly α emission, which is often used to derive spectroscopic redshifts, also suffers resonant scattering. As such, to derive redshifts for each galaxy, we adopt the following approach.

1. Wherever possible, systemic redshifts are determined using nebular emission lines such as H α , [O II] $\lambda\lambda 3726, 3729$, [O III] $\lambda\lambda 4959, 5007$, and/or H β . If none of these lines are available, we use He II or C III $\lambda 1909$ in emission if they are narrow.

2. If no nebular emission lines are detected, we determine the mean of the redshifts from the UV ISM absorption lines of C II $\lambda 1334.53$, Si IV $\lambda 1393.76$, and Si II $\lambda 1526.72$, or other strong emission lines such as N V $\lambda 1240$, Mg II $\lambda 2800$, and He II.
3. If Ly α is the only detected line, then the redshift is determined from a fit to this line, though we caution that the velocity offset from the systemic can be up to $\sim 1000 \text{ km s}^{-1}$. In most of the galaxies where a redshift is determined solely from Ly α , the observations were taken with VIMOS using the low-resolution ($R \sim 180$) grating, precluding any detailed analysis to determine the shape of the emission line and judge the influence of absorption on its observed profile. Similarly, where possible, we avoid using C IV $\lambda 1549$ for measuring the redshifts, since it can be strongly influenced by winds and frequently exhibits a profile that is a superposition of P-Cygni emission and absorption, nebular emission, and interstellar absorption (or AGN activity).

For the ALESS SMGs, $\sim 30\%$ of the redshifts are determined from a single line and generally these redshifts are allocated $Q = 3$ unless strong continuum features (such as breaks across Ly α) are also identified, which leads to an unambiguous identification and a higher quality flag. Single line redshifts are typically backed up by either continuum breaks across Ly α , the absence of other emission lines that would correspond to a different redshift, line profiles (i.e., asymmetric Ly α profile or identifying the doublet of [O II] $\lambda\lambda 3726, 3729$ Å emission). In seven cases, single line redshifts are based on detections of Ly α ; in three cases, they are determined from H α detections in near-infrared spectra and in five cases they are from detections of the [O II] doublet.

We summarize the main spectroscopic features that we detect in Table 3 and provide detailed information on each of the 109 observed SMGs in Table 2.

In Figure 3, we compare our precise spectroscopic measurements for the ALESS SMGs to the photometric redshift estimates for these SMGs from Simpson et al. (2014) who determine photometric redshifts for 77 of the ALESS SMGs which have 4–19 band photometry. We flag those sources with spectroscopic redshifts, but poor photometric coverage and we also highlight the spectroscopic $Q = 3$ redshifts since their spectroscopic identification is often guided by the photometric redshifts. Nevertheless, even if these $Q = 3$ SMGs are omitted, there is good agreement between the photometric and spectroscopic redshifts with a median $\Delta z / (1 + z_{\text{spec}}) = 0.00 \pm 0.02$ and a variance of $\sigma^2 = 0.1$. In four cases, there appear to be significant outliers, with $|\Delta z / (1 + z_{\text{spec}})| > 0.5$. In these cases, the large offset between the photometric and spectroscopic redshifts appears to be associated with complex systems or incomplete photometric coverage, and we briefly discuss these here.

1. ALESS 006.1: the photometry of this ALESS SMG appears to be contaminated by an adjacent low-redshift (and unassociated) AGN, and in this case it appears that the SMG is lensed. The photometry (and photometric redshift) is dominated by the foreground AGN.
2. ALESS 010.1: the $Q = 1$ spectroscopic redshift is significantly lower than predicted by the photometry. There is a blue source slightly offset ($< 1''$) from the ALMA position and an IRAC source coincident with the

¹⁸ Our goal is to provide a quality flag that allows users to gauge the likely success of (or interpret) follow-up observations on a source. For example, a non-detection of the ^{12}CO emission in a $Q = 1$ source should be interpreted as ^{12}CO faint, whereas a ^{12}CO non-detection of a $Q = 3$ source may be due to the faintness of the ^{12}CO emission, or due to a misidentified/spurious redshift.

Table 2
ALESS Spectroscopic Redshift Catalog

ALESS ID	R.A. (J2000)	Decl. (J2000)	z_{spec}	Q_{spec}	z_{phot}^a	M/S ^b	Instruments ^c	Notes
ALESS 001.1	53.310270	-27.937366	4.9540	3	$4.34^{+2.66}_{-1.43}$	M	GMX	[O II] in M-K
ALESS 001.2	53.310059	-27.936562	...	4	$4.65^{+2.34}_{-1.02}$	M	FVX	BLANK
ALESS 001.3	53.309069	-27.936759	...	4	$2.85^{+0.20}_{-0.30}$	M	X	BLANK
ALESS 002.1	53.261188	-27.945211	2.1913	3	$1.96^{+0.27}_{-0.20}$	M	DV	poss. C III] em in D
ALESS 002.2	53.262800	-27.945252	...	4	...	M	D	BLANK
ALESS 003.1	53.339603	-27.922304	4.2373	3	$3.90^{+0.50}_{-0.59}$	M	FMV	poss. Ly α em in F+V
ALESS 003.2	53.342461	-27.922486	...	4	$1.44^{+0.43}_{-0.38}$	S	M	BLANK
ALESS 003.3	53.336294	-27.920555	...	4	...	S	M	BLANK
ALESS 003.4	53.341644	-27.919379	...	4	...	S	M	BLANK
ALESS 005.1	52.870467	-27.985840	...	4	$2.86^{+0.05}_{-0.04}$	M	DMX	BLANK
ALESS 006.1	53.237331	-28.016856	2.3338	1	$0.45^{+0.06}_{-0.04}$	M	GX	cont. from bright sources above SMG; Ly α em ($z = 2.3295$) and C IV em ($z = 2.3314$) in X-UVB; H α and [O III]5007 in G ($z = 2.3338$)
ALESS 007.1	53.314242	-27.756750	2.6923	1	$2.50^{+0.12}_{-0.16}$	M	DFXS	strong cont.; z from H α in X-NIR; He II in X-VIS ($z = 2.6901$)
ALESS 007.2	53.312522	-27.758499	...	4	...	S	D	BLANK
ALESS 009.1	53.047244	-27.869981	...	4	$4.50^{+0.54}_{-2.33}$	M	D	BLANK
ALESS 010.1	53.079418	-27.870781	0.7616	1	$2.02^{+0.09}_{-0.09}$	M	FV	[O II] in V; [O II] ($z = 0.7613$), [O III]4959 ($z = 0.7619$), H β ($z = 0.7617$) in F; z is mean from [O II], [O III], H β , possible lens
ALESS 011.1	53.057688	-27.933403	2.6832	2	$2.83^{+1.88}_{-0.50}$	M	FV	Ly α em in V, no cont.
ALESS 013.1	53.204132	-27.714389	...	4	$3.25^{+0.64}_{-0.46}$	M	DG	BLANK
ALESS 014.1	52.968716	-28.055300	...	4	$4.47^{+2.54}_{-0.88}$	M	VX	BLANK
ALESS 015.1	53.389034	-27.991547	...	4	$1.93^{+0.62}_{-0.33}$	M	DFGVX	BLANK
ALESS 015.2	53.391876	-27.991724	...	4	...	S	M	BLANK
ALESS 015.3	53.389976	-27.993176	3.4252	3	...	M	DM	Ly α em ($z = 3.4399$) and C IV em ($z = 3.4106$) in D
ALESS 015.6	53.388192	-27.995048	...	4	...	S	M	BLANK
ALESS 017.1	53.030410	-27.855765	1.5397	1	$1.51^{+0.10}_{-0.07}$	M	DFMV	strong cont.; z from H α in M-H; Mg II abs in F ($z = 1.5382$)
ALESS 017.2	53.034437	-27.855470	2.4431	3	$2.10^{+0.65}_{-1.37}$	S	M	poss. H α in M-K
ALESS 017.3	53.030718	-27.859423	...	4	$2.58^{+0.16}_{-0.32}$	S	D	BLANK
ALESS 018.1	53.020343	-27.779927	2.2520 ^d	1	$2.04^{+0.10}_{-0.06}$	M	V	cont. in V; archival z from Casey+11
ALESS 019.1	53.034401	-27.970609	...	4	$2.41^{+0.17}_{-0.11}$	M	FV	BLANK
ALESS 020.1	53.319834	-28.004431	...	4	$2.58^{+0.16}_{-0.32}$	S	DFV	cont. in F
ALESS 020.2	53.317807	-28.006470	...	4	...	S	D	BLANK
ALESS 022.1	52.945494	-27.544250	...	4	$1.88^{+0.18}_{-0.23}$	M	FV	cont. in F+V
ALESS 023.1	53.050039	-28.085128	...	4	$4.99^{+2.01}_{-2.55}$	M	V	BLANK
ALESS 025.1	52.986997	-27.994259	2.8719	3	$2.24^{+0.07}_{-0.17}$	M	V	Ly α + break, cont.
ALESS 029.1	53.403749	-27.969259	1.438 9	2	$2.66^{+2.94}_{-0.76}$	M	DGMV	H α in M-H
ALESS 031.1	52.957448	-27.961322	...	4	$2.89^{+1.80}_{-0.41}$	M	FVX	BLANK
ALESS 034.1	53.074833	-27.875910	2.5115	2	$1.87^{+0.29}_{-0.32}$	S	M	broad H α in M-K
ALESS 035.1	52.793776	-27.620948	...	4	...	M	V	BLANK
ALESS 037.2	53.401514	-27.896742	2.3824	3	$4.87^{+0.22}_{-0.40}$	M	M	H α ($z = 2.3824$) and [S II] ($z = 2.3831$)
ALESS 038.1	53.295153	-27.944501	...	4	$2.47^{+0.11}_{-0.05}$	S	D	strong cont. + emission lines from contaminating source
ALESS 039.1	52.937629	-27.576871	...	4	$2.44^{+0.17}_{-0.23}$	M	X	poss. faint lines, no cont.
ALESS 041.1	52.791959	-27.876850	2.5460	2	$2.75^{+4.25}_{-0.72}$	M	FV	strong cont. in F+V; C III]1909 em ($z = 2.5459$), C II]2326 em ($z = 2.5500$) in F; cont. break in V
ALESS 041.3	52.792927	-27.878001	...	4	...	M	M	weak cont.
ALESS 043.1	53.277670	-27.800677	...	4	$1.71^{+0.20}_{-0.12}$	M	DFV	possible faint lines, no cont.
ALESS 043.3	53.276120	-27.798534	...	4	...	S	D	BLANK
ALESS 045.1	53.105255	-27.875148	...	4	$2.34^{+0.26}_{-0.67}$	M	FV	no cont.; poss. Ly α em $z = 2.9690$ from V and C IV $z = 2.9867$ from F
ALESS 046.1	53.402937	-27.547072	...	4	...	S	FV	faint cont. in F
ALESS 049.1	52.852998	-27.846406	2.9417	2	$2.76^{+0.11}_{-0.14}$	M	DFV	strong cont. in F+V; He II em ($z = 2.9417$), C IV em ($z = 2.9436$),
ALESS 049.2	52.851956	-27.843914	...	4	$1.47^{+0.07}_{-0.10}$	M	M	BLANK
ALESS 051.1	52.937754	-27.740922	1.3638	3	$1.22^{+0.03}_{-0.06}$	M	FV	strong cont. in F+V, [O II] ($z = 1.3638$) and break $\sim 8000 \text{ \AA}$ and poss. Mg II em ($z = 1.3681$) in F

Table 2
(Continued)

ALESS ID	R.A. (J2000)	Decl. (J2000)	z_{spec}	Q_{spec}	$z_{\text{phot}}^{\text{a}}$	M/S^{b}	Instruments ^c	Notes
ALESS 055.1	53.259242	-27.676513	1.3564	2	$2.05^{+0.15}_{-0.13}$	M	DF	strong cont. in F+D; Mg II em ($z = 1.3556$) and H+K abs. (Kabs. $z = 1.3572$) in F
ALESS 055.2	53.258983	-27.678148	...	4	...	M	D	BLANK
ALESS 057.1	52.966348	-27.890850	2.9369^{d}	1	$2.95^{+0.05}_{-0.10}$	M	FV	cont. + Ly α em ($z = 2.9387$), C IV em ($z = 2.9332$), He II em ($z = 2.9388$) in V
ALESS 059.2	53.265897	-27.738390	...	4	$2.09^{+0.78}_{-0.29}$	M	X	BLANK
ALESS 061.1	53.191128	-28.006490	4.4190	1	$6.52^{+0.36}_{-0.34}$	M	A	ALMA [C II]158 μm
ALESS 062.1	53.150677	-27.580258	...	4	...	S	D	BLANK
ALESS 062.2	53.152410	-27.581619	1.3614	1	$1.35^{+0.08}_{-0.11}$	S	DFV	[O II] in D+F. [O II] doublet resolved in D.
ALESS 063.1	53.285193	-28.012179	...	4	$1.87^{+0.10}_{-0.33}$	M	G	poss. faint em lines
ALESS 065.1	53.217771	-27.590630	4.4445	1	...	M	AD	z from ALMA [C II]158 μm , Ly α
ALESS 066.1	53.383053	-27.902645	2.5542	1	$2.33^{+0.05}_{-0.04}$	M	FMV	H α and [N II] in M; lensed?
ALESS 067.1	53.179981	-27.920649	2.1230^{d}	1	$2.14^{+0.05}_{-0.09}$	M	FVX	cont. in F+V; H α , [O III]5007 in X-NIR; merging with 067.2
ALESS 067.2	53.179253	-27.920749	2.1230	3	$2.05^{+0.15}_{-0.13}$	M	X	BLANK but likely merging with 067.1
ALESS 068.1	53.138888	-27.653770	...	4	...	M	VX	BLANK
ALESS 069.1	52.890731	-27.992345	4.2071	3	$2.34^{+0.27}_{-0.44}$	M	D	single line, poss. Ly α with asymmetric profile
ALESS 069.2	52.892226	-27.991361	...	4	...	M	M	BLANK
ALESS 069.3	52.891524	-27.993990	...	4	...	M	DM	BLANK
ALESS 070.1	52.933425	-27.643200	2.0918	3	$2.28^{+0.05}_{-0.06}$	M	FX	strong cont. in F; poss. Ly α in X-UVB
ALESS 071.1	53.273528	-27.557831	3.6967	2	$2.48^{+0.21}_{-0.11}$	M	V	Ly α ($z = 3.7006$); very bright line; N V em ($z = 3.6927$)
ALESS 072.1	53.168322	-27.632807	...	4	...	M	DX	poss. faint lines, no cont.
ALESS 073.1	53.122046	-27.938807	4.7649^{d}	1	$5.18^{+0.43}_{-0.45}$	M	DF	very broad Ly α and N V em in D+F; Ly α ($z = 4.7648$), N V ($z = 4.7649$)
ALESS 074.1	53.288112	-27.804774	...	4	$1.80^{+0.13}_{-0.13}$	M	DFV	BLANK
ALESS 075.1	52.863303	-27.930928	2.5450	1	$2.39^{+0.08}_{-0.06}$	M	FVX	very interesting source; strong cont. in V+F; [O III]4959 ($z = 2.5452$), [O III]5007 ($z = 2.5447$) broad red components to [O III], H β ($z = 2.5451$), [O II] doublet ($z = 2.5446$), H α ($z = 2.5452$), Ly α in X ($z = 2.5440$)
ALESS 075.2	52.865276	-27.933116	2.2944	2	$0.39^{+0.02}_{-0.03}$	S	DM	H α , [N II] ($z = 2.2941$), [S II] ($z = 2.2886$) in M-K
ALESS 075.4	52.860715	-27.932144	...	4	$2.10^{+0.29}_{-0.34}$	M	DM	BLANK
ALESS 076.1	53.384731	-27.998786	3.3895	2	...	M	DFMV	[O III]5007 + [O III]4959 in M; poss. Ly α ($z \sim 3.3984$) in V
ALESS 079.1	53.088064	-27.940830	...	4	$2.04^{+0.63}_{-0.31}$	M	D	BLANK
ALESS 079.2	53.090004	-27.939988	1.7693	1	$1.55^{+0.11}_{-0.18}$	M	FVX	Strong H α , [N II]6548, 6583 in X-NIR; structured lines-2 components
ALESS 079.4	53.088261	-27.941808	...	4	...	M	D	BLANK
ALESS 080.1	52.928347	-27.810244	4.6649	3	$1.96^{+0.16}_{-0.14}$	M	FV	poss Ly α in F
ALESS 080.2	52.927570	-27.811376	...	4	$1.37^{+0.17}_{-0.08}$	M	D	BLANK
ALESS 080.5	52.923654	-27.806318	1.3078	3	...	S	D	tentative [O II] + [Ne III]
ALESS 081.1	52.864805	-27.744336	...	4	$1.70^{+0.29}_{-0.20}$	S	V	BLANK
ALESS 082.1	53.224989	-27.637470	...	4	$2.10^{+3.27}_{-0.44}$	M	DFV	BLANK
ALESS 084.1	52.977090	-27.851568	3.9651	3	$1.92^{+0.09}_{-0.07}$	M	DFM	Ly α ($z = 3.9639$), N V ($z = 3.9672$) in F; cont. in F
ALESS 084.2	52.974388	-27.851207	...	4	$1.75^{+0.08}_{-0.19}$	M	DF	cont. in F; poss faint lines
ALESS 087.1	53.212016	-27.528187	2.3086	1	$3.20^{+0.08}_{-0.47}$	M	FV	Ly α em ($z = 2.3188$), Si IV abs ($z = 2.3050$), Si II abs ($z = 2.3019$) in V; Ly α offset from cont.
ALESS 088.1	52.978175	-27.894858	1.2679	1	$1.84^{+0.12}_{-0.11}$	M	FVMX	[O II] ($z = 1.2679$); [O II]3726,3729 visible in X-VIS
ALESS 088.2	52.980797	-27.894529	2.5192	3	...	M	DM	C II]2326 em ($z = 2.5227$), C IV em ($z = 2.5156$) in D
ALESS 088.5	52.982524	-27.896446	2.2941	2	$2.30^{+0.11}_{-0.50}$	M	DFV	strong cont. in V, poss break; Ly α em ($z = 2.3021$), He II ($z = 2.2941$) in V
ALESS 088.11	52.978949	-27.893785	2.3583	3	$2.57^{+0.04}_{-0.12}$	M	D	C III] em ($z = 2.3585$), Ly α em ($z = 2.3581$) + break
ALESS 089.1	53.202879	-28.006079	0.6830	3	$1.17^{+0.06}_{-0.15}$	S	F	bright [O II] + cont
ALESS 094.1	53.281640	-27.968281	...	4	$2.87^{+0.37}_{-0.64}$	M	DV	BLANK
ALESS 098.1	52.874654	-27.956317	1.3745^{d}	1	$1.65^{+0.17}_{-0.09}$	M	DFMVX	[O II] ($z = 1.3745$) brightest in F; cont. in M and F, real H α under sky in X-NIR
ALESS 099.1	53.215910	-27.925996	...	4	...	M	D	BLANK
ALESS 101.1	52.964987	-27.764718	2.7999	2	$3.49^{+0.52}_{-0.88}$	S	V	Ly α

Table 2
(Continued)

ALESS ID	R.A. (J2000)	Decl. (J2000)	z_{spec}	Q_{spec}	$z_{\text{phot}}^{\text{a}}$	M/S ^b	Instruments ^c	Notes
ALESS 102.1	53.398333	-27.673061	2.2960	3	$1.76^{+0.16}_{-0.18}$	M	FV	cont. in V, Ly α ($z = 2.2931$), C III] ($z = 2.2960$) in V
<i>ALESS 106.1</i>	<i>52.915187</i>	<i>-27.944236</i>	...	4	$7.00^{+0.00}_{-4.07}$	S	DM	BLANK
ALESS 107.1	52.877082	-27.863647	2.9965	3	$3.75^{+0.09}_{-0.08}$	M	VM	Ly α em ($z = 2.9757$), C IV em ($z = 2.9965$) in V; cont. in V+M; poss. [O II], [O III] in M
ALESS 107.3	52.878013	-27.865465	...	4	$2.12^{+1.54}_{-0.81}$	M	D	BLANK
ALESS 110.1	52.844411	-27.904784	...	4	$2.55^{+0.70}_{-0.50}$	M	FMV	BLANK
ALESS 110.5	52.845677	-27.904005	...	4	...	M	DM	BLANK
ALESS 112.1	53.203596	-27.520362	2.3154	1	$1.95^{+0.15}_{-0.26}$	M	FGV	Ly α em ($z = 2.3122$) + cont. in V, H α ($z = 2.3145$), poss [O III]5007 ($z = 2.3157$), H β em ($z = 2.3160$) in G
ALESS 114.2	52.962945	-27.743693	1.6070	1	$1.56^{+0.07}_{-0.07}$	M	FV	strong cont in F+V, [O II] doublet in F ($z = 1.6070$)
ALESS 115.1	53.457070	-27.709609	3.3631	3	...	M	V	cont., poss Ly α em ($z = 3.3631$)
ALESS 116.1	52.976342	-27.758039	...	4	$3.54^{+1.47}_{-0.87}$	M	FV	BLANK
ALESS 116.2	52.976826	-27.758735	...	4	$4.02^{+1.19}_{-2.19}$	M	F	BLANK
ALESS 118.1	52.841347	-27.828161	2.3984	3	$2.26^{+0.50}_{-0.23}$	M	DFV	strong cont in F+V, Ly α abs + break, C IV em ($z = 2.3984$) in V
ALESS 119.1	53.235993	-28.056988	...	4	$3.50^{+0.95}_{-0.35}$	M	V	BLANK
ALESS 122.1	52.914768	-27.688792	2.0232 ^d	1	$2.06^{+0.05}_{-0.06}$	M	FV	very strong blue cont. and abs. lines. V: C II] abs ($z = 2.0197$), Si IV abs ($z = 2.0229$), He II em ($z = 2.0282$), Very broad C IV and Si II blended abs.; C III] ($z = 2.0222$). F: Fe II 2344, Fe II 2375, Fe II 2383 abs
ALESS 124.1	53.016843	-27.601769	...	4	$6.07^{+0.94}_{-1.16}$	M	FV	poss faint lines
ALESS 126.1	53.040033	-27.685466	...	4	$1.82^{+0.28}_{-0.08}$	M	V	BLANK

Notes. The 22 ALESS SMGs not targeted in our spectroscopy program (and without redshifts from the literature) are not listed here. The SUPP SMGs are shown in italics. $z_{\text{spec}} = -99$ means that we could not determine a spectroscopic redshift.

^a Photometric redshifts from S14. Those SMGs without a photometric redshift have poor photometric constraints (detections in <4 bands).

^b M = MAIN catalog, S = SUPP catalog.

^c F = VLT/FORS2, V = VLT/VIMOS, X = VLT/XSHOOTER, M = Keck/MOSFIRE (Band *H* or *K*), D = Keck/DEIMOS, G = Gemini/GNIRS.

^d These redshifts are for the six sources that also have literature spectroscopic redshifts described in Section 3. The quality flag (Q) for the spectroscopic redshifts is $Q = 1$ for secure redshifts; $Q = 2$ for redshifts measured from only one or two strong lines; $Q = 3$ for tentative redshifts measured based on one or two very faint features; $Q = 4$ for those sources that were targeted but no redshift could be determined.

(This table is available in machine-readable form.)

ALMA position. *HST* imaging (Chen et al. 2015) reveals two galaxies and it is possible that the blue source is a lens, as confirmed by high-resolution, $\sim 0''.1$ ALMA band 7 follow-up observations; (Hodge et al. 2016).

- ALESS 037.2: the $Q = 3$ spectroscopic redshift is significantly lower than the $z > 4$ predicted by the photometry. However, the spectroscopic redshift is based on two tentative line detections at the correct separation for H α and [S II] (see Figure 2; [N II], if present, would lie under strong sky lines) and the photometric redshift is poorly constrained and based on detections in six bands and limits in a further six. Furthermore, the spectroscopic line identifications would not correspond to any common emission lines if the photometric redshift is correct.
- ALESS 101.1: this has a $Q = 2$ redshift based on a single detection of Ly α . It has poor constraints on the photometric redshift with photometric detections in only five bands and no detections below *J*-band. Thus the spectroscopic redshift is significantly more reliable.

For a significant fraction of the ALMA sample targeted in our survey, we were unable to derive a spectroscopic redshift (these are assigned $Q = 4$ in Table 2). To understand whether

this is caused by magnitude limits or their redshifts, we first compare the photometric redshifts of the spectroscopic failures to those for the SMGs for which we were able to determine a spectroscopic redshift. The median photometric redshift of spectroscopic failures is $z = 2.4 \pm 0.2$, compared to $z = 2.4 \pm 0.1$ for the sources for which we were able to measure a spectroscopic redshift (these estimates use the best-fit photometric redshift values, but they change by less than the quoted uncertainty if the full photometric redshift probability distributions are used instead). This suggests that the SMGs with spectroscopic failures are not at much higher redshifts than those SMGs where we have succeeded in obtaining a redshift. Similarly, there does not appear to be any correlation with submillimeter flux: for the 52 SMGs with spectroscopic redshifts, the median 870 μm flux is $S_{870 \mu\text{m}} = 4.2^{+0.3}_{-0.4}$ mJy, whereas those 57 SMGs where we could not determine a redshift have a median $S_{870 \mu\text{m}} = 4.3^{+0.2}_{-0.6}$ mJy.

Next, we test the hypothesis that we were unable to measure spectroscopic redshifts for some ALMA SMGs simply due to their faint optical magnitudes. In Figure 4, we show the distributions of the $S_{870 \mu\text{m}}$ flux density, *R*-band and 4.5 μm magnitudes, and 1.4 GHz flux density for the 109 (out of 131) ALESS SMGs that were spectroscopically

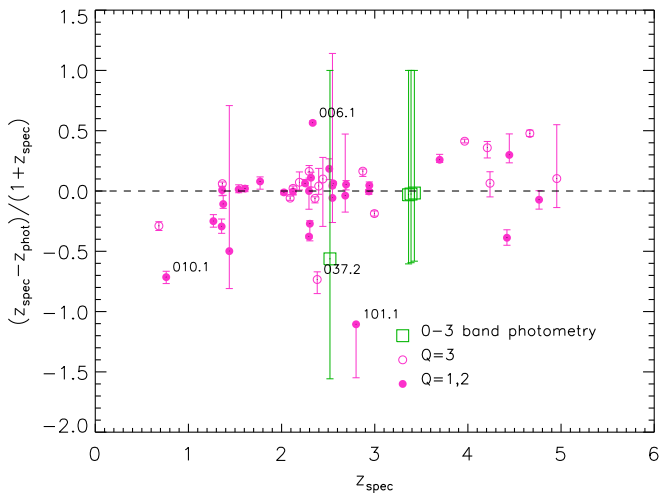


Figure 3. Comparison of our spectroscopic redshifts for ALESS SMGs with their estimated photometric redshifts from Simpson et al. (2014). Overall, the photometric redshifts agree well with our spectroscopic redshifts with a median $\Delta z / (1 + z_{\text{spec}}) = 0.00 \pm 0.02$. The errors represent the uncertainties on the photometric redshifts determined from the SED fitting in Simpson et al. (2014). We identify those SMGs with detections in just 0–3 photometric bands where the redshift has been determined by assuming these SMGs have an absolute H -band magnitude distribution comparable to that of a complete sample of $z \sim 1$ –2 SMGs. SMGs with photometric redshift estimated from only 0–1 and 2–3 band photometry are placed at the median for those sources of $z \sim 4.5$ and $z \sim 3.5$ respectively.

targeted. The median R -band magnitude of the ALESS SMGs with spectroscopic redshifts is $R = 24.0 \pm 0.2$, whereas the median magnitude of those SMGs for which we could not measure a redshift is ~ 1 mag fainter, at $R = 25.0 \pm 0.4$. Turning to longer wavelengths, in the mid-infrared, the median magnitude at $4.5 \mu\text{m}$ is $m_{4.5 \mu\text{m}} = 20.9 \pm 0.2$ for the ALESS SMGs with spectroscopic redshifts, as compared to a median of $m_{4.5 \mu\text{m}} = 21.7 \pm 0.2$ for those targeted SMGs for which we could not derive a spectroscopic redshift. Hence, there is evidence that the ALESS SMGs for which we were unable to determine a spectroscopic redshift are marginally fainter in R and $m_{4.5 \mu\text{m}}$ than those for which we were able to measure a spectroscopic redshift (and also may have slightly redder $R - m_{4.5 \mu\text{m}}$ colors).

In Figure 5, we plot the redshifts of the ALESS SMGs versus their $4.5 \mu\text{m}$ apparent magnitudes. At the typical redshift of SMGs ($z \sim 2.4$), the $4.5 \mu\text{m}$ emission provides the most reliable tracer of the underlying stellar mass, since it corresponds to rest-frame $\sim 1.6 \mu\text{m}$ (H -band). As a guide, to crudely test how the $4.5 \mu\text{m}$ magnitude depends on redshift in our sample, we generate a non-evolving starburst track, based on the composite SED for the ALESS SMGs (shown in Simpson et al. 2014 but updated to contain the spectroscopic redshift information in Figure 9). This model SED has been normalized to the median apparent $4.5 \mu\text{m}$ magnitude for the spectroscopic and photometric redshift samples at the median redshift of $z \sim 2.4$. The dependence of $4.5 \mu\text{m}$ flux with redshift for our spectroscopic sample is consistent with this track, though with a spread of ~ 2 mag at fixed redshift. However, the data do show a trend of decreasing $4.5 \mu\text{m}$ flux with increasing redshift. Smail et al. (2004; see also Serjeant et al. 2003) also identified a similarly large spread in K -band magnitudes for SMGs.

Hence we see both a spread in the apparent rest-frame near-infrared luminosities within the SMG population, as well as the

Table 3
Summary of Spectroscopic Features

Condition	Number of galaxies Total [SUPP]
Total	131 [32]
$Q = 1$	20 [1]
$Q = 2$	11 [3]
$Q = 3$	21 [3]
Redshifts measured	52 [7]
Not observed	22 [10]
Observed but no spec z	57 [15]
$\text{Ly}\alpha$	23 [1]
[O II]	10 [3]
[O III]	6 [0]
$\text{H}\alpha$	14 [3]
[O III] and $\text{H}\alpha$	3 [0]
$\text{H}\beta$	3 [0]

Note. The numbers in brackets represent the number of SUPP SMGs included in the total in each row.

fainter optical apparent magnitudes (and redder colors) for those SMGs that we failed to obtain redshifts for and marginally higher photometric redshifts compared to those for which spectroscopic redshifts were measured. Each of these trends are weak, but they do suggest several factors may be driving the spectroscopic incompleteness: a range in stellar masses for SMGs at a fixed redshift (a demonstration of the diversity of the SMG population), varying levels of strong dust extinction and fainter apparent optical fluxes for SMGs at higher redshifts (due to the K correction and increasing distance).

In terms of the radio-detected sub-sample, from the entire MAIN+SUPP ALESS catalog, 53/131 ALESS SMGs are radio-detected, and we have targeted 52 with spectroscopy, measuring redshifts for 34. The median 1.4 GHz flux density of the SMGs with spectroscopic redshifts is $S_{1.4 \text{ GHz}} = 63_{-13}^{+12} \mu\text{Jy}$ compared to $S_{1.4 \text{ GHz}} = 39_{-2}^{+6} \mu\text{Jy}$ for those without spectroscopic redshifts (Figure 4). Thus, SMGs for which we were unable to determine a spectroscopic redshift are fainter at radio wavelengths than those for which we measured a spectroscopic redshift.

4. Spectroscopic Redshift Distribution

The spectroscopic redshift distribution of the ALESS SMGs is shown in Figure 6. In total, 52 redshifts have been determined for the ALESS SMGs: 45 MAIN catalog SMGs and seven SUPP catalog SMGs. We also overlay the probability density function of the photometric redshift distribution of ALESS SMGs from Simpson et al. (2014), scaled to the same number of sources. The $Q = 1$ and 2 and $Q = 1$ –3 distributions are shown as individual histograms to test the effect of including the $Q = 3$ redshifts. The full redshift distribution ranges between $z = 0.7$ –5.0, with a significant (but not dominant) tail at $z \geq 3$ for those distributions without a radio selection.

In Figure 7, we show the ALESS spectroscopic redshift distribution and compare this with the 1.1 mm selected (U) LIRGs from the recent ALMA surveys of the *Hubble* Ultra Deep Field (UDF) by ASPECS (Aravena et al. 2016; Walter et al. 2016) and Dunlop et al. (2017). Given the different selection wavelengths, flux limits and sample sizes between the

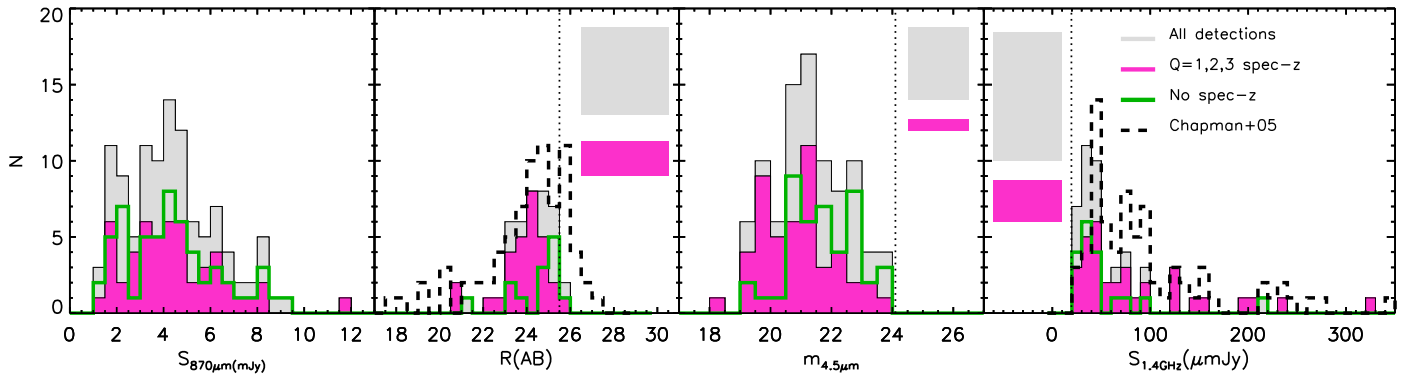


Figure 4. Fundamental observable properties of our spectroscopic sample of SMGs, comprising 870 μm fluxes, R -band and 4.5 μm magnitudes, and 1.4 GHz fluxes. The distributions are compared to those of the parent population of ALESS SMGs (where the parent sample comprises the 109/131 SMGs that were targeted in our spectroscopic survey). In all panels, we show three distributions: for the full sample (with and without spectroscopic redshifts), the properties of the SMGs with $Q = 1, 2,$ or 3 spectroscopic redshifts and the distribution for SMGs with photometry but no spectroscopic redshift. As separate boxes, we also indicate the proportion of the full and spectroscopic samples that are below the detection limit of the observations in each waveband (these 3σ detection limits are indicated by dotted lines in each panel). On average, we find that the SMGs for which we were able to determine a redshift are marginally brighter in the R -band, and $m_{4.5\mu\text{m}}$ than those for which we were unable to determine a redshift, however, the likelihood of determining a redshift is independent of the 870 μm flux density and so our survey is unbiased in this regard. In addition, in the R -band and 1.4 GHz panels, we also show the equivalent distribution for the spectroscopic sample of 73 radio-identified submillimeter sources from Chapman et al. (2005), which exhibit comparable properties to our sample. Note that ALESS 020.1 has a very bright radio flux of ~ 4.2 mJy and is therefore not shown on the 1.4 GHz panel.

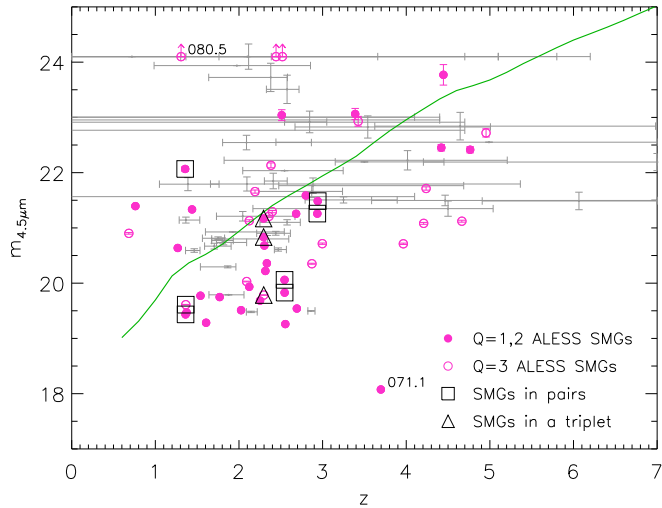


Figure 5. Plot showing the distribution of 4.5 μm apparent magnitude vs. redshift for ALESS SMGs. We see a tendency for more distant SMGs to have fainter 4.5 μm magnitudes and to assess this we plot a line showing the expected variation with redshift for a galaxy with a fixed, non-evolving luminosity, assuming the composite ALESS SED from Simpson et al. (2014) (see also Figure 9). This track is normalized to the median apparent magnitude in 4.5 μm at a median redshift of $z = 2.4$. The data roughly follow this trend, though they exhibit at least an order of magnitude variation in 4.5 μm magnitude at a fixed redshift. Those SMGs that are found to be physically associated (pairs or triples) with other SMGs are highlighted. Those in associations have a marginal tendency to be among the brighter SMGs (and therefore could potentially be more massive; see Section 5.3). Photometric redshifts (where spectroscopic redshifts are not available) are shown as their $\pm 1\sigma$ ranges given in Simpson et al. (2014) and Table 2. The two extreme outliers are identified with their ALESS ID.

ALESS SMGs and the ALMA/UDF galaxies, we caution against drawing strong conclusions about the differences between these redshift distributions (for a detailed discussion see Béthermin et al. 2015). Nevertheless, we note that all of these distributions peak at $z \sim 2.0 \pm 0.5$, with a suggestion that fainter sources may lie at lower redshifts on average.

Before continuing with the analysis, we briefly assess the effect on our sample of including the SUPP SMGs and those

with only $Q = 3$ redshifts. Karim et al. (2013) demonstrate that up to $\sim 30\%$ of the SUPP sources are likely to be spurious. However, SUPP sources that have an optical/near-infrared counterpart have a lower likelihood of being spurious sources. The median redshift of the MAIN catalog SMGs with $Q = 1-3$ redshifts is $z = 2.5 \pm 0.1$ with an interquartile range of $z = 2.1-3.4$, whereas the median redshift of the MAIN+SUPP catalog with $Q = 1-3$ redshifts is $z = 2.4 \pm 0.1$ with an interquartile range of $z = 2.1-3.0$. The median redshift of the $Q = 1-3$ SMGs in the SUPP sample alone is $z = 2.3 \pm 0.5$. Thus, the median redshifts of these various samples are all consistent. Indeed, a two-sided Kolmogorov–Smirnov (K–S) test between the MAIN and SUPP samples suggests only a 60% likelihood that they are drawn from different populations. Since the statistics of the samples do not vary strongly with the inclusion of the SUPP sources, we are therefore confident that including the SUPP sources in our analyses is unlikely to bias any of our results.

Since most previous SMG redshift surveys have, by necessity, relied on radio detections to identify probabilistically the likely counterparts, we briefly discuss the properties of the radio-detected subset of the ALESS SMGs because this provides a reasonable comparison to previous work. In our sample, we targeted 52 of the 53 radio-detected SMGs with spectroscopy and measured redshifts for 34 of them (65%). The median 1.4 GHz radio flux density of the 34 radio-detected ALESS SMGs with spectroscopic redshifts is $63^{+12}_{-13} \mu\text{Jy}$, as compared to $50^{+6}_{-5} \mu\text{Jy}$ for all 52 radio-detected SMGs. In contrast, the median radio flux density of the 73 radio-detected submillimeter sources in Chapman et al. (2005) with spectroscopic redshifts is $75^{+8}_{-3} \mu\text{Jy}$. On average, the radio-detected ALESS SMGs with redshifts are $\sim 20\%$ fainter at 1.4 GHz than the Chapman et al. (2005) sample and our spectroscopic completeness is $\sim 10\%$ lower. We note that it appears that the Chapman et al. (2005) radio-identified submillimeter sources have a higher AGN fraction than our ALESS sample, and indeed up to $\sim 40\%$ of their sample exhibits signatures of AGN activity in the X-rays, spectra, or from their broadband optical/mid-infrared SEDs (e.g., Alexander et al. 2008;

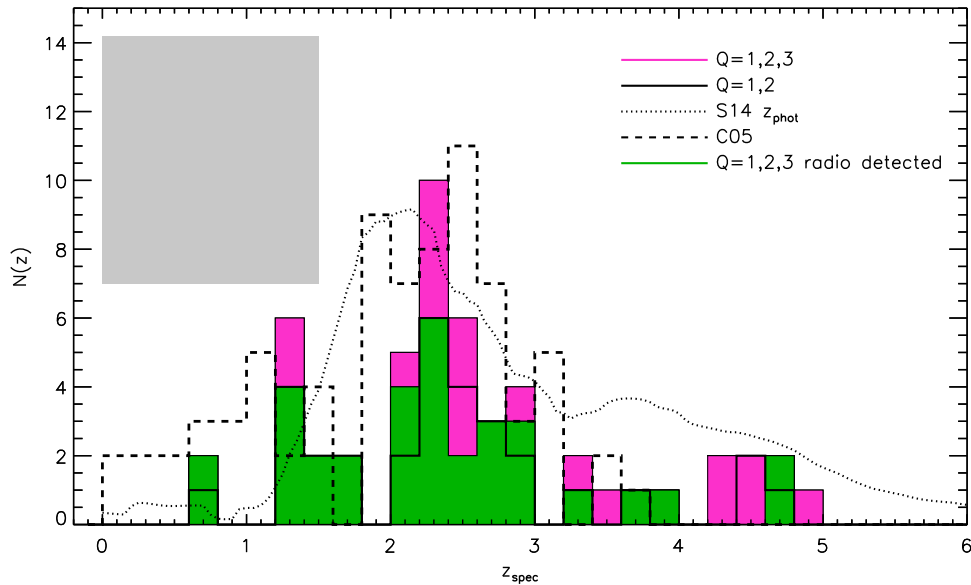


Figure 6. Spectroscopic redshift distribution of the SMGs from our survey. Those SMGs with secure redshifts ($Q = 1$ and 2) are shown, as well as the distribution for all $Q = 1$ – 3 redshifts. We compare the distribution to the probability density function of the photometric redshifts from Simpson et al. (2014) normalized to the same total number of sources. We also compare to the redshift distribution of radio-identified submillimeter sources from Chapman et al. (C05, 2005). We see very striking differences between the ALESS SMG redshift distribution and that for Chapman et al. (2005), both at low and high redshifts, $z \lesssim 1$ and $z \gtrsim 3.5$. In particular, the ALESS SMGs have a spectroscopic redshift distribution that extends to higher redshift, with $\sim 23\%$ of the SMGs at $z > 3$ and an even larger proportion in the more complete, but less precise, photometric redshift distribution from Simpson et al. (2014). To mimic the selection of the radio-identified Chapman et al. (2005) sample, the redshift distribution of the radio-detected ALESS SMGs are highlighted. This shows that there are still discernable differences between the redshift distributions of the radio-detected ALESS SMGs and those from Chapman et al. (2005) at low redshifts, $z \lesssim 1$, raising the possibility that some of the low-redshift radio counterparts to submillimeter sources claimed by Chapman et al. (2005) could be misidentifications. The bin size is $\Delta z = 0.2$ and the gray shaded box indicates the incompleteness in the $Q = 1$ – 3 sample compared to the parent population of targeted SMGs in the field.

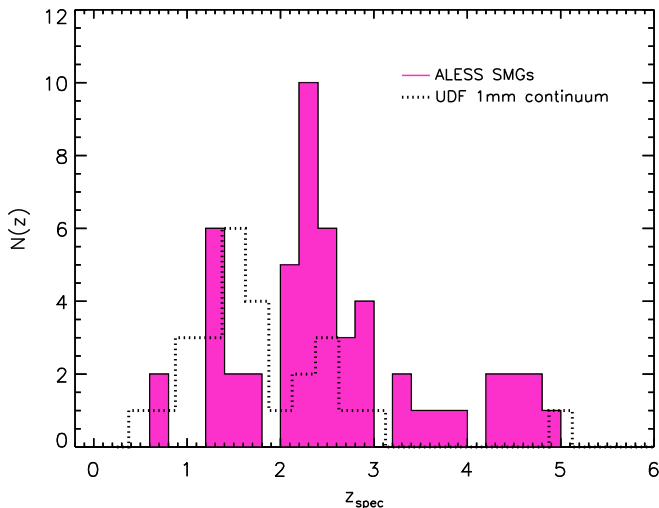


Figure 7. Spectroscopic redshift distribution of the SMGs in our $870 \mu\text{m}$ survey compared to that for two faint 1.1 mm selected samples in the UDF from Aravena et al. (2016) and Dunlop et al. (2017; we note that the total number of sources for the distributions shown are not the same). These SMG samples have quite different selection functions and levels of incompleteness and so we do not draw any strong conclusions from the apparent differences between them, beyond noting that both distributions peak at relatively high redshifts, $z \sim 1.5$ – 2.5 , and reach out to $z \sim 5$ with the more numerous ALESS $870 \mu\text{m}$ sample showing a more significant high-redshift tail beyond $z \sim 3$.

Hainline et al. 2011). Wang et al. (2013) find an AGN fraction of $\sim 17_{-6}^{+16}\%$ for the ALESS SMGs. Typically, AGN spectra have stronger, more easily identifiable emission features and thus our $\sim 10\%$ lower spectroscopic completeness may be due to a lower AGN fraction.

5. Discussion

Although the primary aim of this work is to determine the redshifts of unambiguously identified SMGs to support further detailed follow-up (e.g., CO or $\text{H}\alpha$ dynamics, e.g., Huynh et al. 2013), there is also a wealth of information contained within the spectra themselves concerning the dynamics, chemical composition, and energetics of these SMGs. Furthermore, the redshifts can be used as constraints in SED models (e.g., constraining the star formation history and thus the stellar masses) and to investigate the environments in which these SMGs reside.

5.1. Spectral Diagnostics

5.1.1. Stacked Spectral Properties

Stacked spectra are a useful tool to detect weak features that are not visible in individual spectra and also for determining the average properties of the population. We therefore produce composite spectra over two different wavelength ranges, one covering $\text{Ly}\alpha$ and UV ISM lines and one around the $[\text{O II}] \lambda 3727$ and Balmer break, and we use these to search for evidence of emission/absorption features and continuum breaks. To construct the composites, we first transform each spectrum to the rest-frame using the best redshift in Table 2. Where the sky subtraction leaves significant residuals, the region within $\pm 5 \text{ \AA}$ of the sky lines is masked before stacking (and we use the OH line catalog from Rousselot et al. 2000 to identify the bright sky lines in the near-infrared). We then sum the spectra, inverse weighted by the noise (measured as the standard deviation in the region of continuum over which they have been normalized). In the case of the 1000 – 2000 \AA composite (Figure 8), we normalize the spectra by their median

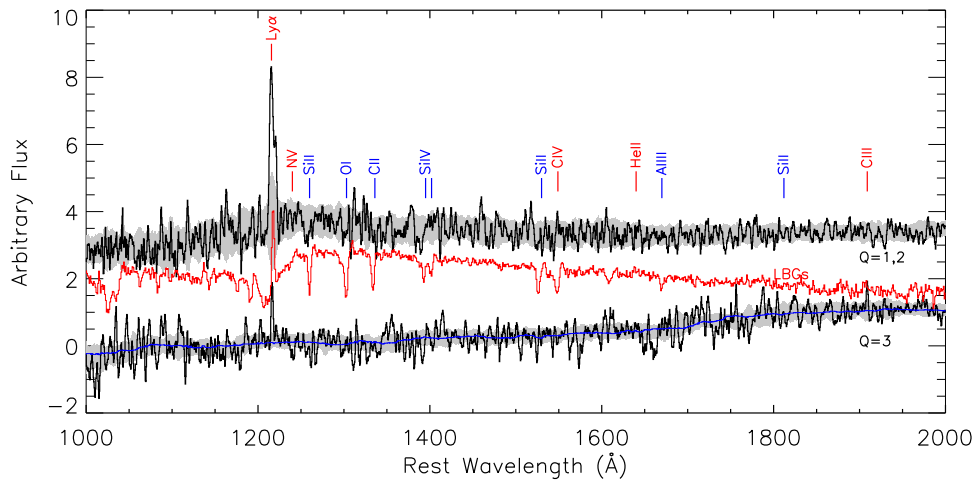


Figure 8. Composite spectra around the $\text{Ly}\alpha$ emission line ($\sim 1215 \text{ \AA}$). The spectra are averaged and weighted by their noise and the uncertainty is derived from bootstrap resampling of the spectra included in the stack and is shown as the gray shaded regions. The upper spectrum shows the stack of all the $Q = 1$ and 2 spectra, which shows a number of potential absorption features, as well as the $\text{Ly}\alpha$ emission line. For comparison, the composite spectrum of LBGs from Shapley et al. (2003) is overlaid in red (and offset for clarity). The $Q = 3$ stack at the bottom was produced to test the validity of the uncertain $Q = 3$ redshifts by identifying features in their composite spectrum. The solid blue line is a running median of the $Q = 3$ composite. We see apparently significant detections of $\text{Ly}\alpha$ and a weak feature, which may be $\text{C III } \lambda 1909$ in the $Q = 3$ composite and, if real, may indicate that some of these redshifts are correct.

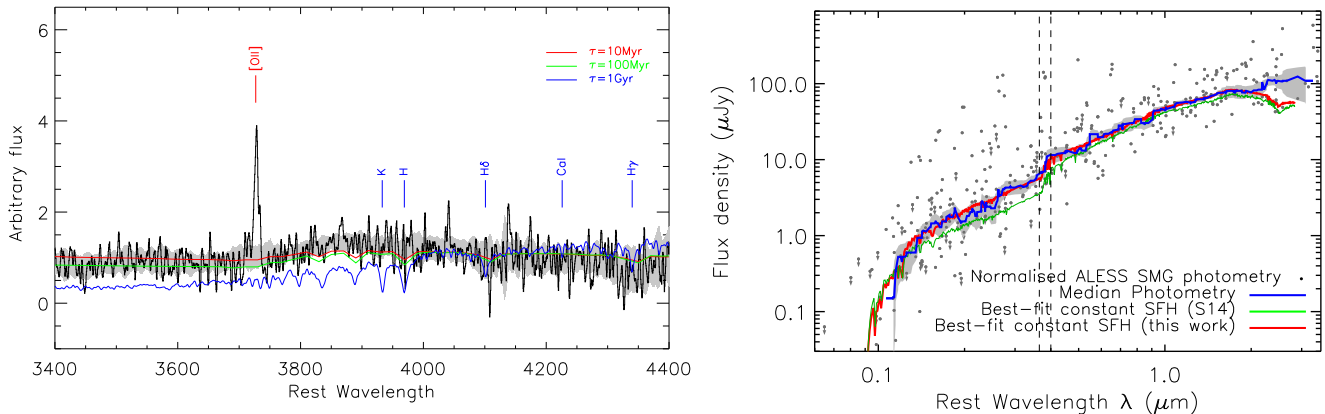


Figure 9. Left: the composite spectrum covering restframe 3400–4400 \AA of the $Q = 1$ and 2 ALESS spectra with the X-ray AGN removed from the sample. This shows strong $[\text{O II}]$ emission and potentially $\text{H}\delta$ absorption, as well as the presence of a spectral break around $\sim 3800 \text{ \AA}$ resulting from the Balmer series. We overlay model spectra for a continuous 100 Myr starburst observed at 10, 100, and 1000 Myr. The model spectra for the 10 Myr burst provides the closest match to the strength of the Balmer break. The spectra were normalized by their median continuum flux between 2900 and 3600 \AA and sky-subtracted by the same method as in Figure 8. We show the uncertainty in the composite derived from a bootstrap resampling of the sources included in the composite as a gray shaded region. Right: a composite SED using the photometry from Simpson et al. (S14, 2014) for those ALESS SMGs with $Q = 1$ –3 spectroscopic redshifts. The photometry for each source has been de-redshifted and normalized by their rest-frame H -band luminosity. The solid line represents the running median of 20 points per bin. The shaded region indicates the bootstrap error on the running median. The red curve represents the best-fit model SED, assuming a constant star formation rate to the average photometry for all ALESS SMGs, whereas the green curve is the equivalent model fit taken from Simpson et al. (2014). The de-redshifted photometry and limits are shown as gray points and arrows respectively. The vertical dashed lines indicate the Balmer (3646 \AA) and 4000 \AA breaks.

continuum value at $>1250 \text{ \AA}$ and in the case of the composite around 3400–4400 \AA (Figure 9), we normalize by the median continuum value between 2900–3600 \AA . We note that when transforming the spectra to the rest-frame, in a number of cases, the UV ISM lines and $\text{Ly}\alpha$ can be significantly offset in velocity from this systemic redshift (see Figure 12). In the composite spectrum, these spectral features may therefore appear broadened and offset.

We first discuss the composite spectra of the region around $\text{Ly}\alpha$, 1000–2000 \AA , see Figure 8. We show a composite constructed from just the $Q = 1$ and 2 spectra, which displays strong $\text{Ly}\alpha$ and a continuum break at $\sim 1200 \text{ \AA}$. The spectrum also shows two Si II absorption lines and apparently offset Si IV absorption, as well as potentially weak C IV absorption and emission and O I absorption. If the feature identified as Si IV is real, then it and the weaker C IV features, both of which show

blueshifts, may be indicative of strong stellar winds. To illustrate the typical strength of the absorption features we also overlay the composite spectrum of ~ 200 Lyman break galaxies (LBGs) from Shapley et al. (2003; the LBG composite shown here corresponds to the quartile of 200 LBGs from the Shapley et al. 2003 sample that has the closest match in $\text{Ly}\alpha$ equivalent width to our ALESS sample). We note that due to the different wavelength ranges of the different instruments used and the fact that we de-redshift and stack in the rest-frame, not all of the spectra in our stack contribute to the full wavelength range.

We also construct a composite from the $Q = 3$ spectra and plot this in Figure 8. The purpose of this is to test the reliability of the redshifts derived for the $Q = 3$ spectra by searching for weak spectral features, which are undetected in the individual spectra, but become visible in the stacked spectrum due to the

improved signal-to-noise. In addition to an emission line identified as Ly α (which is frequently the feature used to derive the redshift for these sources), we see only a potential emission feature that would correspond to C III] λ 1909 and no evidence of a break in the continuum across the bluer emission line. If the C III] λ 1909 emission is real, then it may indicate that some of the $Q = 3$ redshifts are correct.

To search for continuum breaks and absorption lines in the rest-frame optical, and to determine if we can constrain the luminosity weighted age of the stellar populations in SMGs, we also produce a rest-frame composite of the $Q = 1$ and 2 spectra over the wavelength range of 3400–4400 Å (removing the bright X-ray AGN from the sample; Wang et al. 2013) and show this in Figure 9. We detect strong [O II], and potentially also H δ absorption (Figure 9). In addition, we see in this composite that continuum falls off bluewards of ~ 3800 Å. A break in this region could be due to the 4000 Å break, typically observed in older stellar systems, or more likely the Balmer break at ~ 3656 Å. The Balmer break arises in stellar populations, which are either experiencing on-going star formation over the previous >100 Myr, or in post-starburst stellar populations, 0.3–1 Gyr after the strongest star formation has ended (Shapley 2011). In the composite, the position discontinuity is more consistent with the Balmer break than a 4000 Å break because the continuum at 3500–3600 Å is $(1.5 \pm 0.1) \times$ lower than it is at 3900–4000 Å.

To try to place limits on the age of the visible stellar populations within the ALESS SMGs, we use the SED templates from Bruzual & Charlot (2003) to predict the spectra expected from a starburst of 100 Myr duration observed at ages of 10 Myr, 100 Myr, and 1 Gyr (post-starburst). We redden the model spectra using the reddening law from Calzetti et al. (2000), adopting the median extinction of $A_V = 2$ for the ALESS SMGs, as derived from SED fitting (see Section 5.1.2). As Figure 9 shows, the stellar continuum emission seen in the composite spectrum is most similar to an on-going burst (i.e., undergoing star formation on 10–100 Myr timescales), as expected for these strongly star-forming galaxies.

As well as stacking the spectra, we can also create a rest-frame broadband SED for a “typical” SMG (or at least “typical” of the brighter/bluer examples for which redshifts can be measured). Simpson et al. (2014) and Swinbank et al. (2014) discuss the optical/near-infrared and far-infrared/radio photometry of the ALESS SMGs (see also da Cunha et al. 2015). By combining the multi-wavelength photometry with spectroscopic redshifts for the 52 ALESS SMGs, we create composite SEDs from the rest-frame UV to radio wavelengths. First, we transform the photometry to the rest-frame, and then stack the photometry (normalized by rest-frame H -band luminosity; see Section 5.1.2). A running median is then calculated through the data to produce an average SED, which we show in Figure 9. We also overlay a HYPER-Z fit using a constant star formation history, which indicates (as expected) a heavily dust reddened spectrum of these SMGs. Our best-fit constant star formation model shows a slightly bluer continuum than that derived using the photometric redshift sample by Simpson et al. (2014), illustrating a modest bias to bluer restframe UV continua in those SMGs for which we can measure spectroscopic redshifts for. Nevertheless, our spectroscopic composite SEDs still display a very red continuum shape and a clear break at ~ 3800 Å, as seen in the composite spectrum at this wavelength (Figure 9).

5.1.2. UV-to-radio SEDs

Using our sample of spectroscopically confirmed SMGs with extensive UV-to-radio photometry, we employ the MAGPHYS SED fitting code from (see da Cunha et al. 2015) to fit the UV-to-radio emission on a galaxy-by-galaxy basis to estimate the dust reddening, far-infrared luminosity and infer the stellar mass for each SMG. Estimates of these parameters have been made using photometric redshifts, but the addition of spectroscopic redshifts removes some of the degeneracies between photometric redshift, reddening, and star formation histories, to allow more precise estimates to be made. The UV–mid-infrared photometry for the ALESS SMGs is given in Simpson et al. (2014), while the (deblended) *Herschel*/SPIRE+PACS, ALMA and radio photometry are given in Swinbank et al. (2014) (see also da Cunha et al. 2015). For each SMG, we use MAGPHYS to fit the photometry at the spectroscopic redshift, and we show the best-fit SEDs (normalized by their 8–1000 μm luminosities) in Figure 10.¹⁹ These normalized, rest-frame SEDs demonstrate a large range in the UV- to optical-flux density, which is driven by a large spread in the dust attenuation. Indeed, the estimated extinction varies from $A_V \sim 0.5$ –7 mag between SMGs (see also da Cunha et al. 2015).

From the sample, we derive a median extinction of $A_V = 1.9 \pm 0.2$ and far-infrared luminosity of $L_{\text{FIR}} = (3.2 \pm 0.4) \times 10^{12} L_{\odot}$, both of which are consistent with previous estimates (for the same sample) derived using photometric redshifts ($A_V = 1.7 \pm 0.2$ and $L_{\text{FIR}} = (3.5 \pm 0.4) \times 10^{12} L_{\odot}$, respectively, from Simpson et al. 2014). In addition, MAGPHYS also returns estimates of the stellar masses (solving for the star formation histories and ages) and we derive a median stellar mass for our 52 SMGs with spectroscopic redshifts of $M_{\star} = (6 \pm 1) \times 10^{10} M_{\odot}$, in agreement with previous estimates for this sample using photometric redshifts and simple assumptions about the star formation histories by Simpson et al. (2014), see also da Cunha et al. (2015). This is also consistent with the stellar mass estimates for the radio-identified submillimeter sources in the Chapman et al. (2005) sample ($M_{\star} \sim 7 \times 10^{10} M_{\odot}$; Hainline et al. 2011). In Figure 11, we plot the ALESS SMGs with spectroscopic redshifts on the stellar mass–star formation rate plane. For comparison, we overlay the trends proposed for the so-called “main sequence” of star forming galaxies at $z = 1$ –3 and compare these to the SMGs in the same redshift slices. From this plot, it is clear that the SMGs in our sample lie (on average) a factor of ~ 5 above the so-called “main sequence” at all three redshifts, with a median specific star formation rates (sSFR) of $\text{sSFR} = (6 \pm 1) \times 10^{-9} \text{ yr}^{-1}$ (see also, e.g., Magnelli et al. 2012; Simpson et al. 2014).

5.2. Velocity Offsets between Emission/Absorption Lines

Rest-frame UV optical spectroscopic analysis of high-redshift, star-forming galaxies have shown that redshifts derived from UV ISM absorption lines typically display systematic blueshifted offsets from the systemic (nebular) redshifts (e.g., Erb et al. 2006; Steidel et al. 2010; Martin et al. 2012), while redshifts determined from Ly α emission often show a systematic offset redward of the systemic. These velocity offsets are a consequence of large-scale outflows (e.g., Pettini

¹⁹ The template SEDs are available from <http://astro.dur.ac.uk/~ams/zLESS/>.

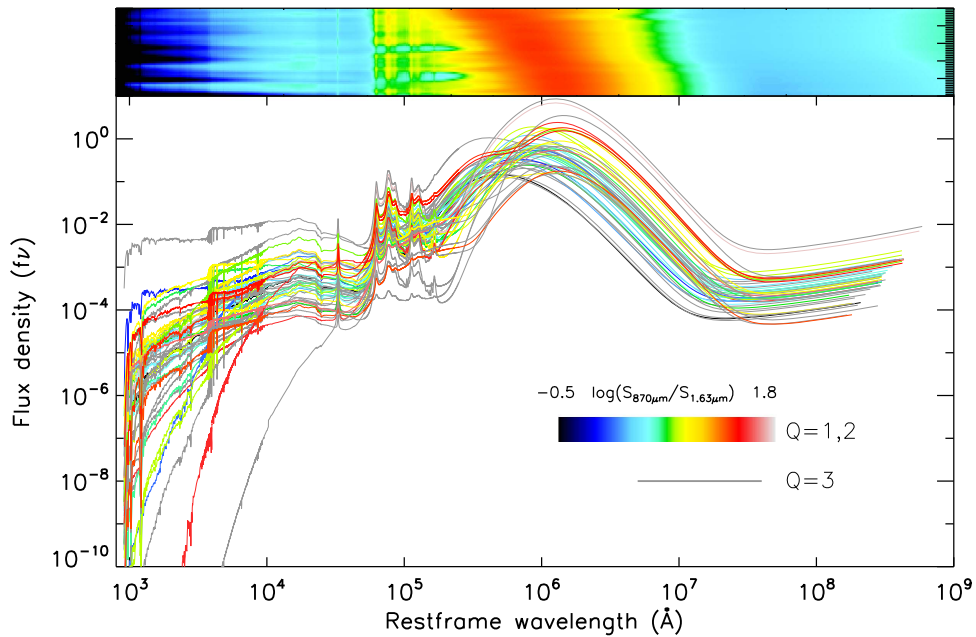


Figure 10. Best-fit rest-frame SEDs for all ALESS SMGs with spectroscopic redshifts. These SEDs have been fitted using MAGPHYS (see da Cunha et al. 2008) and are normalized by their far-infrared (8–1000 μm) luminosity. The colored curves represent SEDs for SMGs with $Q = 1$ and 2 redshifts. They are color coded by the logarithm of their ratio of rest-frame $S_{870\ \mu\text{m}}/H$ flux density (with red denoting a higher ratio). Gray curves represent SEDs for SMGs with $Q = 3$ redshifts. We see a very large spread in the UV to optical flux density arising from a large spread in the attenuation. The color scale in the upper image shows the 52 SEDs ranked by their characteristic dust temperature. These illustrate the wide variety in both the restframe UV/optical/near-infrared and mid-infrared characteristics of SMGs with very similar far-infrared luminosities.

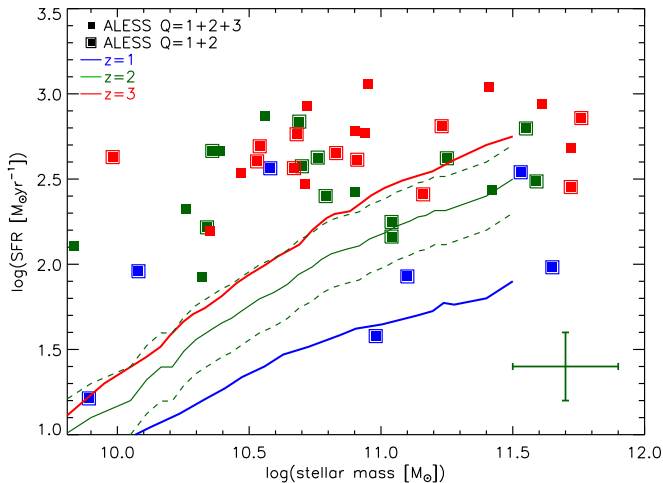


Figure 11. Stellar mass–star formation rate plane for ALESS SMGs with spectroscopic redshifts compared to the so-called “main sequence” of star-forming galaxies at $z = 1$ –3. We identify the ALESS SMGs with the best spectroscopic redshifts ($Q = 1$ and 2) and the points are color coded by their spectroscopic redshift. Taken at face value, the plot suggests that at $z \sim 1$ –3 SMGs have sSFRs that lie between the “main sequence” and an order of magnitude higher sSFR and on average their sSFR are a factor of $\sim 5\times$ higher than the bulk of the star-forming population at their stellar mass. However, we caution that the stellar masses of these highly obscured and strongly star-forming galaxies are systematically uncertain (Hainline et al. 2011). We illustrate the expected conservative uncertainties for the measurements by the error bars plotted in the lower-right of the panel and stress that it is possible that the SMGs could be moved systematically by comparable amounts on this figure.

et al. 2002; Steidel et al. 2010), where the outflow material between the galaxy and the observer absorbs the UV and scatter $\text{Ly}\alpha$ photons from the receding outflow, redshifting them with respect to the neutral medium within the galaxies.

For some of the ALESS SMGs, we are able to determine nebular, UV ISM and $\text{Ly}\alpha$ redshifts, allowing us to compare to the results for other star-forming populations.

In Table 2, we summarize the lines detected for each ALESS SMG and the redshift associated with fitting to each line. We show the velocity offsets between the $\text{Ly}\alpha$, UV ISM, and nebular emission lines in Figure 12. We also overlay the velocity offsets for the radio-identified counterparts to submillimeter sources studied by Chapman et al. (2005). Though the same trend is seen in the SMGs and LBGs ($\text{Ly}\alpha$ is redshifted and the UV ISM lines are blueshifted with respect to the systemic redshift), the SMGs display significantly more scatter, with velocity offsets ranging between ~ -1100 to $+700\ \text{km s}^{-1}$ for the UV ISM-derived redshifts and between ~ -1500 to $+1200\ \text{km s}^{-1}$ for the $\text{Ly}\alpha$ -derived redshifts, as compared to -600 to $+100\ \text{km s}^{-1}$ and $\sim +100$ to $+900\ \text{km s}^{-1}$, respectively, for the LBGs in Steidel et al. (2010). The wide variation in the velocity offsets may be due to a spread in the viewing angle of the winds or the presence of multiple components (Chen et al. 2015 suggest that most SMGs are major mergers and so the spectra may have contributions from merging components), or the diversity of conditions within these SMGs, in particular, with regard to the strength of large-scale winds. Since the wind must be accelerated by star formation or AGN activity, in Figure 12, we plot the velocity offsets between lines as a function of bolometric luminosity (we note that only two SMGs in our sample are X-ray AGNs; Wang et al. 2013 and neither of these show $\text{Ly}\alpha$ and UV ISM lines with extreme offsets from the systemic redshift). Although there is significant scatter within the ALESS sample, the SMGs with lower bolometric luminosity tend to have wind velocities that are lower than those of the highest luminosity sources.

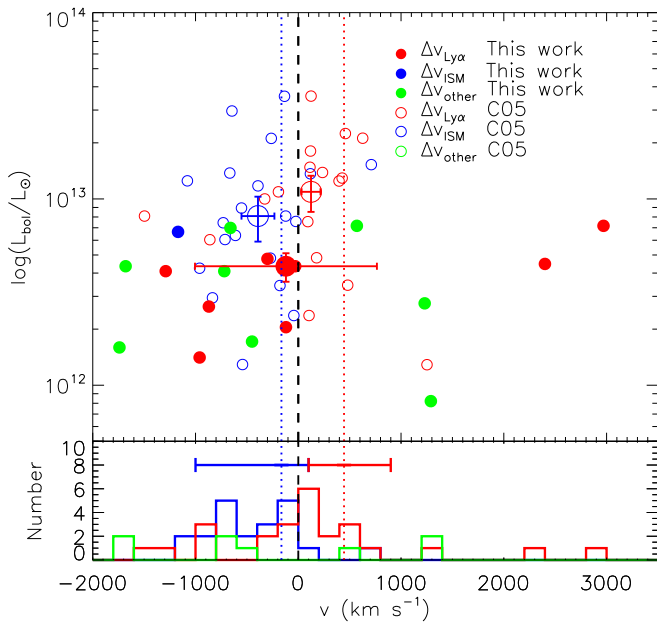


Figure 12. Top: velocity offsets of the UV ISM absorption lines and Ly α from the systemic redshifts (marked by the dashed line) vs. bolometric luminosity ($L_{8-1000\ \mu\text{m}}$) for all ALESS SMGs and the radio-identified submillimeter sources from Chapman et al. (2005), where appropriate lines are detected. The median of each sample is marked by a larger symbol. The red and blue dotted lines represent the mean of the distributions of Ly α and ISM velocity offsets, respectively, from the $z = 2-3$ LBG study from Steidel et al. (2010) and the full range are shown as error bars on the bottom figure. We show a representative error bar for our data derived from the median error on the bolometric luminosity and we estimate a typical redshift measurement error of $\sim 100\ \text{km s}^{-1}$ from fitting the spectral lines. The green points indicate offsets measured between lines that can be either nebular or ISM lines and are frequently strongly influenced by winds, such as C IV $\lambda 1549$, N V $\lambda 1240$, C III] $\lambda 1909$, Mg II $\lambda 2800$, and He II. Note that the far-infrared luminosities for the Chapman et al. (2005) sources are derived from their radio fluxes and may be overestimated. Bottom: histograms of the distributions of velocity offsets for Ly α (red), UV ISM lines (blue), and other lines (green). The histograms include the SMGs from ALESS and the radio-identified submillimeter sources in Chapman et al. (2005), and demonstrate that Ly α and the UV ISM lines in SMGs do indeed, respectively, peak redward and blueward of the systemic velocity, as expected if these systems are driving outflows and winds.

We note that the outliers in Figure 12 are ALESS 088.5 and ALESS 049.1, with Ly α offset from the systemic by $>2000\ \text{km s}^{-1}$. For both ALESS 088.5 and ALESS 049.1 the only line available to determine a nebular/systemic velocity was He II $\lambda 1640$, which, as we described previously, can originate from the stellar winds from Wolf-Rayet stars, making it less reliable as a systemic velocity tracer than the typical nebular lines (e.g., H α). It is important to note that the nebular lines such as H α , [O III], and [O II] may also be influenced by winds; however, this is more typically observed as line broadening as opposed to a centroid shifting.

5.3. Environments

One of the key benefits from obtaining spectroscopic redshifts for SMGs is the capability they provide to study both the small- and larger-scale environments of these sources. Hence, we next use our spectroscopic redshift sample to search for physical associations between SMGs and between SMGs and other galaxy populations within the field. Various studies have investigated the environments of SMGs and suggested that at least some SMGs reside within overdense environments (e.g.,

Chapman et al. 2001; Blain et al. 2004; Chapman et al. 2009; Daddi et al. 2009; Capak et al. 2011; Walter et al. 2012; Ivison et al. 2013; Decarli et al. 2014; Smolcic et al. 2017). For example, Blain et al. (2004; see also Chapman et al. 2009) identified an over-density of six SMGs and two radio galaxies at $z = 1.99$ within $1200\ \text{km s}^{-1}$ of each other in the GOODS-N field. Clustering analysis has also suggested that SMGs cluster on scales of $5-10\ h^{-1}\ \text{Mpc}^{-1}$, while pair counting suggests SMGs have properties consistent with them evolving into the passive red galaxies at $z \sim 1$, and subsequently the members of rich galaxy groups or clusters at $z \sim 0$ (e.g., Blain et al. 2004; Hickox et al. 2012; Chen et al. 2016; Wilkinson et al. 2017).

A potentially related result was found by Karim et al. (2013), who demonstrated that single dish submillimeter sources suffer significant “multiplicity” (see also Simpson et al. 2015b, with $>35\%$ of the single dish sources resolved into multiple SMGs (where an SMG is a far-infrared bright galaxy with an $870\ \mu\text{m}$ flux brighter than $1\ \text{mJy}$). Simpson et al. (2015b) also showed that the number density of $S_{870} \gtrsim 2\ \text{mJy}$ SMGs in ALMA maps of bright single-dish submillimeter sources is ~ 80 times higher than that derived from blank-field counts. After taking into account the observational biases in their sample, they proposed that an over-abundance of faint SMGs of this magnitude is inconsistent with line-of-sight projections dominating multiplicity in the brightest SMGs, and strongly suggests that a significant proportion of these high-redshift ULIRGs are likely to be physically associated. These SMGs are typically separated by $\sim 6''$, which corresponds to $\sim 40-50\ \text{kpc}$ if they lie at the same redshift.

With our survey, we can use a simple approach and exploit the spectroscopic redshifts to search for associations and overdensities in the ALESS SMG population. First, we search for physical associations between SMGs in the same ALMA map (i.e., within $\sim 18''$), where the SMGs lie within $2000\ \text{km s}^{-1}$ (though an offset of $2000\ \text{km s}^{-1}$ is larger than the typical velocity dispersion of rich clusters, even at $z \sim 0$, we broaden our search window to account for potential outflow-driven shifts in the spectral features used to derive the redshifts of many of the SMGs (see Section 5.2). Unfortunately, there are only three ALESS maps in which we were able to determine a reliable spectroscopic redshift for two or more of the SMGs (ALESS 017.1, 017.2; 075.1, 075.2; 088.1, 088.2, 088.5, and 088.11), and in none of these maps do we find any small-scale clustering of SMGs along the line of sight, the range of redshift offsets between these (previously blended) components is $\Delta z = 0.06-1.25$. Only in ALESS 067 do we have indirect evidence for an interacting pair of SMGs (ALESS 067.1 and ALESS 067.2) based on the morphology of the sources in *HST* imaging (Chen et al. 2015).

Next, we search for physical associations between SMGs across the whole ECDFS field (i.e., between the ALMA maps). We identify seven pairs of SMGs within $2000\ \text{km s}^{-1}$ of each other, with ALESS 075.2, ALESS 088.5, and ALESS 102.1 also appearing as a triple “association.” These pairs/triples of SMGs have an average offset of $\sim 4\ \text{Mpc}$ in the plane of the sky (with a range of $\sim 2-15\ \text{Mpc}$). On these scales, the pairs (or triples) may lie within the same large-scale structure but are unlikely to lie within the same dark matter halos.

To determine whether these potential “associations” correlate with redshift peaks in other galaxy populations, we compare the spectroscopic redshift distribution of the ALESS SMGs with that of the infill targets from our survey, as well as

other archival surveys. Most of the spectroscopic redshifts for the other galaxy populations were taken from an updated version of the redshift compilation in Luo et al. (2011) listing >15,000 spectroscopic redshifts for galaxies in the ECDFS with a median redshift of $z \sim 0.67$ and an interquartile range of $z = 0.3\text{--}1.0$.²⁰ From this catalog, we select only secure redshifts and remove duplicates (we also remove cases in which two secure but differing redshifts are given from two different references).

In Figure 13, we plot the spectroscopic redshift distribution of the ALESS SMGs, together with the field population. In those cases where ≥ 2 SMGs lie within 2000 km s^{-1} , these associations do not often statistically coincide with significant overdensities in the background galaxy population, though the two SMGs at $z \sim 1.36$ are coincident with a slight peak in the radio/MIPS sources at that redshift.

Finally, returning to Figure 5, we have highlighted there the 10 SMGs that are members of pairs (or triples) with spectroscopic redshift offsets between components of $\leq 2000 \text{ km s}^{-1}$. The median apparent magnitude at $4.5 \mu\text{m}$ for these 10 SMGs is $m_{4.5 \mu\text{m}} = 20.4_{-0.6}^{+0.7}$ as compared to a median of $m_{4.5 \mu\text{m}} = 21.1_{-0.4}^{+0.1}$ for the 42 ALESS SMGs in the parent spectroscopic sample, which are not in identified “associations.” We conclude that there is no evidence in the current sample that the SMGs in “associations” are any brighter (and thus potentially more massive) than those not in “associations.”

6. Conclusions

In this work, we present the results from a redshift survey of ALMA-identified SMGs. Our main conclusions are as follows.

1. The redshift distribution for ALESS SMGs with spectroscopic redshifts is centered at $z = 2.4 \pm 0.1$, but with a full range of $z = 0.7\text{--}5.0$ and an interquartile range of $z = 2.1\text{--}3.0$. This is consistent with the photometric redshift distribution for these sources, and the median is consistent with previous estimates based on the radio-identified counterparts to submillimeter sources (Chapman et al. 2005). However, since we do not rely on a radio selection, our sample is not biased against higher redshift SMGs and indeed, 23% of the ALESS SMGs with spectroscopic redshifts lie at $z > 3$.
2. We identify velocity offsets up to $\sim 3000 \text{ km s}^{-1}$ between the redshifts measured from nebular emission lines (i.e., $\text{H}\alpha$, $[\text{O III}]$, $\text{H}\beta$, and $[\text{O II}]$) and those measured from $\text{Ly}\alpha$ or UV ISM absorption lines. We conclude that it is likely that the extreme SFRs within the SMGs (typically $\sim 300 \pm 30 M_{\odot} \text{ yr}^{-1}$) are driving strong galaxy-scale outflows in many of these systems.
3. Since many of our spectra of SMGs are too faint to exhibit any obvious emission or absorption features

(continuum is only detected in $\sim 50\%$ of the sources), we produce composite spectra over various wavelength ranges to search for weaker features in the “typical” ALESS SMG optical-to-near-infrared spectrum. At rest-frame $1000\text{--}2000 \text{ \AA}$, we see strong, asymmetric $\text{Ly}\alpha$ emission, and blueshifted Si II and potentially Si IV absorption suggestive of strong stellar winds. Our composite spectrum at rest-frame $3400\text{--}4400 \text{ \AA}$ shows a Balmer break, indicative of on-going star formation. Comparing our composite to spectral models, we suggest that it is most consistent with a young starburst with an age of $\sim 10 \text{ Myr}$.

4. We use our precise spectroscopic redshifts to reduce the uncertainties when modeling the SEDs of our SMGs using MAGPHYS and find a large spread in the dust attenuation ($A_V \sim 0.5\text{--}7 \text{ mag}$) with a median $A_V = 1.9 \pm 0.2$. We also derive a median stellar mass of $M_{\star} = (6 \pm 1) \times 10^{10} M_{\odot}$ and by combining with our estimates of their star formation rates, we show that SMGs lie (on average) ~ 5 times above the so-called “main sequence” at $z \sim 1\text{--}3$. We provide this library of template SEDs for 52 SMGs with precise redshifts and well-sampled photometry as a resource for future studies of SMGs.

This work has highlighted the challenges of measuring spectroscopic redshifts at optical-to-near-infrared wavelengths for dusty star-forming galaxies identified by ALMA, and thus demonstrates the importance of alternative methods of measuring redshifts such as mid-infrared spectroscopy (e.g., Valiante et al. 2007) and the increasing importance of blind submillimeter/millimeter spectral searches with ALMA (e.g., Weiß et al. 2013).

Nevertheless, we find that the SMG population is a diverse population of dusty galaxies most common at $z \sim 2.4$, with evidence of energetic outflows, which are likely to be predominantly driven by star formation, though some may have a contribution from AGNs. The main goal of this study was to provide redshifts for subsequent studies such as CO gas or further detailed integral field unit follow-up observations. Such studies will allow us to separate out the relative contributions of star formation and AGNs, to probe the conditions within the star-forming gas to better understand this extreme and diverse population of galaxies.

We acknowledge the ESO programs 183.A-0666 and 090.A-0927(A). The ALMA observations were carried out under program 2011.0.00294.S. A.L.R.D. acknowledges an STFC studentship (ST/F007299/1) and an STFC STEP award. A.M. S. gratefully acknowledges an STFC Advanced Fellowship through grant ST/H005234/1, STFC grant ST/L00075X/1 and the Leverhulme foundation. I.R.S. acknowledges support from STFC, a Leverhulme Fellowship, the ERC Advanced Investigator program DUSTYGAL 321334 and a Royal Society/Wolfson Merit Award. W.N.B. acknowledges STScI grant HST-GO-12866.01-A. C.M.C. acknowledges support from a McCue Fellowship at the University of California, Irvines Center for Cosmology, and the University of Texas at Austin’s College of Natural Science. J.L.W. is supported by a European Union COFUND/Durham Junior Research Fellowship under EU grant agreement number 267209. A.K. acknowledges support by the Collaborative Research Council 956, sub-project A1, funded by the Deutsche Forschungsgemeinschaft (DFG). ALMA is a

²⁰ http://www.eso.org/sci/activities/garching/projects/goods/MASTERCAT_v3.0.dat, which includes redshifts from Cristiani et al. (2000), Croom et al. (2001), Bunker et al. (2003), Dickinson et al. (2004), Stanway et al. (2004a, 2004b), Strolger et al. (2004), Szokoly et al. (2004), van der Wel et al. (2004), Le Fèvre et al. (2005), Doherty et al. (2005), Mignoli et al. (2005), Ravikumar et al. (2007), Vanzella et al. (2008), Popesso et al. (2009), Balestra et al. (2010), Coppin et al. (2010), Silverman et al. (2010), Kurk et al. (2013); and redshifts also taken from Kriek et al. (2008), Boutsia et al. (2009), Taylor et al. (2009), Treister et al. (2009), Wuyts et al. (2009), Casey et al. (2011), Xia et al. (2011), Bonzini et al. (2012), Cooper et al. (2012), Coppin et al. (2012), Iwasawa et al. (2012), Mao et al. (2012), Le Fèvre et al. (2013), Georgantopoulos et al. (2013), De Breuck et al. (2014), Williams et al. (2014), and the 2dF Galaxy Redshift Survey (Colless et al. 2003).

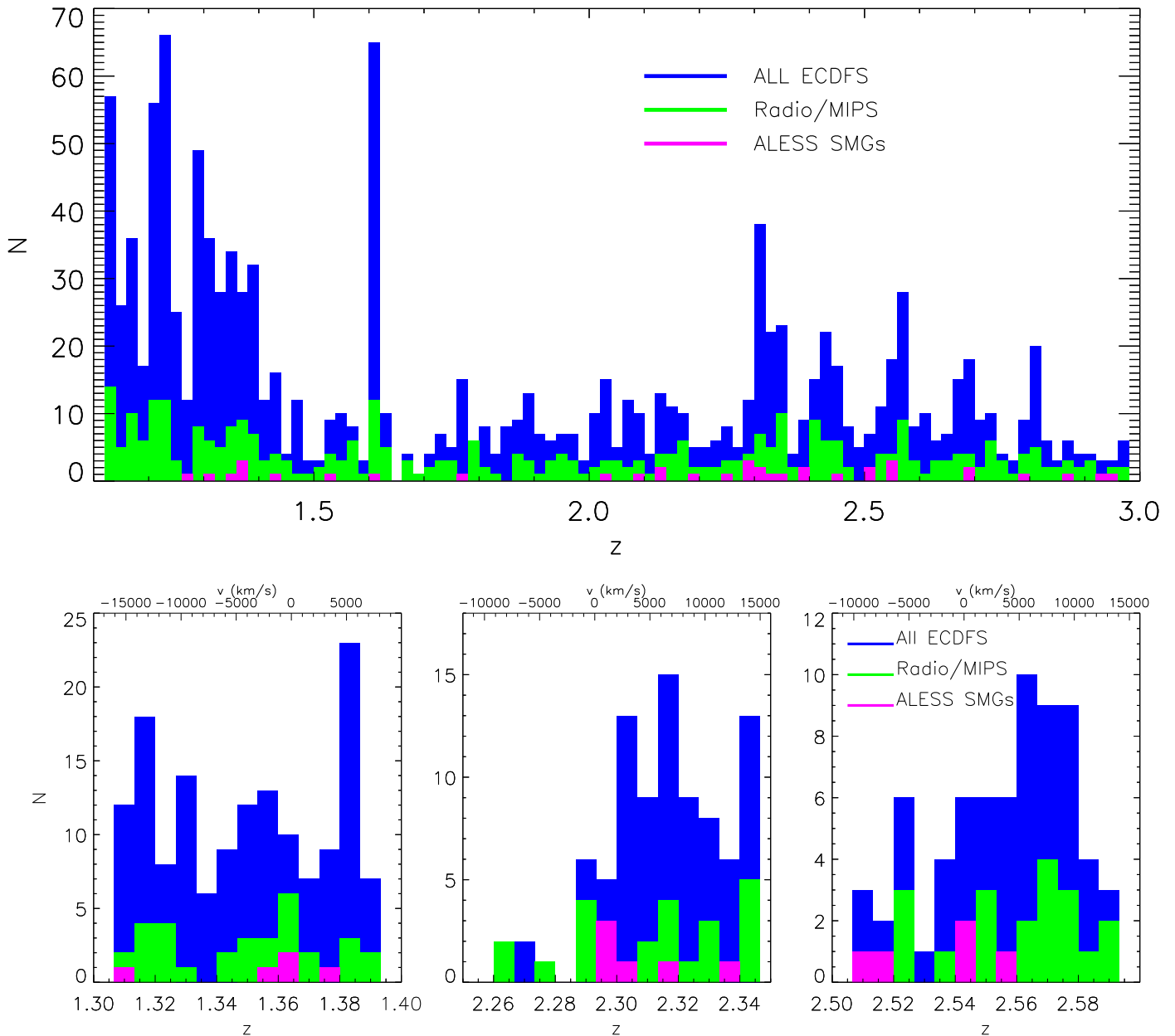


Figure 13. Top: the spectroscopic redshift distribution of SMGs ($Q = 1-3$) compared to the less luminous galaxy populations in the field. The latter is based on the catalog compiled by Luo et al. (2011) with the addition of recent redshifts from the full FORS2/VIMOS survey (Table 2) and from Williams et al. (2014). We plot all the galaxies in the ECDFS for which we have spectroscopic redshifts (including the SMGs), we also plot the distributions for just the radio/MIPS sources, as well as the SMGs. We see little correlation between the peaks in the SMG redshift distribution and the general galaxy distribution. The binning is 6000 km s^{-1} in all panels. Bottom: expanded views of the redshift distribution around the associations of the ALESS SMG compared to the overall galaxy redshift distribution. We find a maximum of three SMGs in our adopted 2000 km s^{-1} window, in addition to three pairs of SMGs. The pairs/triples in the SMG population do not obviously coincide with overdensities in the less-active galaxy populations across the field. The color coding is the same as Figure 13 and the top axis indicates velocity relative to the redshift of the pair/triple.

partnership of ESO (representing its member states), NSF (USA) and NINS (Japan), together with NRC (Canada) and NSC and ASIAA (Taiwan), in cooperation with the Republic of Chile. The Joint ALMA Observatory is operated by ESO, AUI/NRAO, and NAOJ.

Appendix A ALESS SMGs with Literature Redshifts

The following sources are ALESS SMGs with previously measured spectroscopic redshifts.

1. ALESS 018.1 is listed as ID 66 in Casey et al. (2011) with a redshift of $z = 2.252$ derived from an $H\alpha$ detection with the Infrared Spectrometer And Array Camera (ISAAC) on the VLT;
2. ALESS 057.1 is listed as ID 112a in Szokoly et al. (2004) with a redshift of $z = 2.940$ derived from detections of He II, O VI, and N V with FORS1/FORS2. It is classed as a QSO with strong high-ionization emission lines;
3. ALESS 067.1 is listed as ECDFS-45 in Kriek et al. (2008) at $z = 2.122$, derived from emission lines in the near-infrared spectrum observed with GNIRS;

4. ALESS 073.1 is listed as GDS J033229.29–275619.5 in the Vanzella et al. (2008) compilation of 1019 spectroscopic redshifts for GOODS/CDFS. The redshift of $z = 4.762$ was determined via the detection of Ly α and N V using FORS2.
5. ALESS 098.1 is identified as IDJ033129 in Casey et al. (2011). The redshift $z = 1.4982$ is derived through a tentative detection of H α ; however, it is also spectroscopically identified in the restframe UV in the same paper and therefore it is given a “secure” status. This redshift is, however, in disagreement with our $Q = 1$ redshift of $z = 1.3735$ derived from fitting to an [O II] line in the FORS2 observations, with a tentative detection of H α at the same redshift under a sky line in the XSHOOTER near-infrared spectrum. We use our redshift in the analysis in this work; and
6. ALESS 122.1 is listed as radio ID 149 in Bonzini et al. (2012). The redshift of $z = 2.03$ is determined from UV ISM absorption features observed with VIMOS.

Appendix B Notable Individual Sources

Since we have a wealth of spectroscopic data, we can utilize the spectra not only for the purpose of determining redshifts but also to search for diagnostic features indicative of AGN activity, star formation, strong stellar winds etc. Here we highlight and discuss some of the most notable, high signal-to-noise spectra.

ALESS 057.1: This SMG hosts a luminous AGN that is detected in X-rays (Wang et al. 2013). The VIMOS spectrum (Figure 2) exhibits strong, broad, symmetric Ly α emission, broad N V and C IV emission (FWHM ~ 3700 km s $^{-1}$), which is significantly blueshifted (~ 1600 km s $^{-1}$) with respect to both He II and Ly α (which have velocities that are consistent within measurements errors). The C IV emission line also displays a P-Cygni profile.

ALESS 066.1: This SMG is listed as an X-ray AGN at $z = 1.310$ in Wang et al. (2013). However, our observations reveal the optical/near-infrared photometry and X-ray emission are dominated by a foreground QSO at $z = 1.310$, but our near-infrared spectroscopy with MOSFIRE identifies an emission line in *K*-band slightly to the north of the QSO. At $\lambda = 2.333$ μ m, this line corresponds to H α at $z = 2.5542$. Careful analysis of the ALMA and optical imaging reveals that the SMG is indeed $\lesssim 1''$ north of the QSO and hence is likely to be lensed by the foreground QSO.

ALESS 073.1: This SMG also hosts a luminous X-ray AGN (Vanzella et al. 2008; Coppin et al. 2009; Wang et al. 2013; De Breuck et al. 2014) and the spectrum (Figure 2) shows strong, broad N V with an FWHM ~ 3000 km s $^{-1}$ as compared to a relatively narrow and weak Ly α (FWHM ~ 700 km s $^{-1}$).

ALESS 075.1: We have excellent spectroscopic coverage of this SMG and have strong detections of [O II], [O III] $\lambda 4959$, 5007, H β , and H α with XSHOOTER. The H α detection is narrow with FWHM ~ 160 km s $^{-1}$. The [O III] emission is not fit well with a single Gaussian because it is an asymmetric line with a red wing, possibly indicating an outflow (e.g., Alexander et al. 2010). Given the high [O III] luminosity and the lack of an X-ray detection, this outflow may be accelerated by an obscured AGN (i.e., outflows in high-redshift ULIRGs hosting AGN activity; Harrison et al. 2012).

ALESS 079.2: This SMG has strong detections of H α and [N II] with XSHOOTER. The one- and two-dimensional spectra show structured emission (see Figure 14). In the one-dimensional spectrum, the H α and [N II] lines are truncated at their red end and appear to be more extended toward lower velocities. The flux ratio of [N II] $\lambda 6583$ /H α is consistent with the ionizing radiation arising from H II regions as opposed to an AGN.

ALESS 087.1: Strong rest-frame UV continuum is detected in this SMG with ISM absorption lines, with reshifts consistent with the Ly α emission line. However, the Ly α is significantly offset northward of the continuum in the two-dimensional spectrum. We therefore extract two spectra in Figure 14 taken from the position of the Ly α and the continuum. The Ly α profile is marginally asymmetric with a truncated blue edge. The continuum spectrum shows an obvious break and relatively strong Si IV absorption. Unfortunately, there is very poor photometric coverage of this SMG (3.6–8 μ m only) so we are unable to say whether the offset Ly α is due to a close companion or an interaction with another system, or a less-obscured part of a single galaxy.

ALESS 122.1: This SMG has very blue continuum with strong UV ISM absorption lines in both the FORS2 and VIMOS spectra (Figure 14). There is very strong, broad C IV absorption (FWHM of > 7000 km s $^{-1}$). The C IV exhibits a strong, narrow component associated with interstellar absorption and a very broad red component associated with stellar winds. The strength of this redshifted component suggests the presence of a large number of very massive stars ($> 30 M_{\odot}$; Leitherer & Heckman 1995). Models show that Si IV is relatively weak for a continuous star formation history but yields a strong P-Cygni profile for bursty star formation. Detection of a P-Cygni profile for Si IV is therefore a good indicator that the burst duration is short relative to the age. The Si IV absorption feature is unusually broad (> 3000 km s $^{-1}$). This is the blueshifted wind absorption. Swinbank et al. (2014) determine $L_{\text{FIR}} = (6.0 \pm 0.4) \times 10^{12} L_{\odot}$ for this SMG, which implies a star formation rate of $\text{SFR} \sim 1040 \pm 70 M_{\odot} \text{ yr}^{-1}$ (using Kennicutt 1998), which is higher than typical ALESS SMGs, $\text{SFR} \sim (310 \pm 30) M_{\odot} \text{ yr}^{-1}$ (Swinbank et al. 2014). We note that an AGN may also exhibit strong C IV absorption and given the very strong continuum and the large width of the C IV in this SMG, it is plausible that it may be a broad absorption line (BAL) AGN.

Appendix C Ancillary Redshifts

When designing the slit masks, we in-filled the unused portions’ masks (not targeting the high-priority SMGs) with other candidate high-redshift galaxies, in particular with mid-, far-infrared, or radio-selected galaxies. Here, we provide the details of the galaxies targeted.

The ID for each galaxy relates to the input catalog from which a target was selected. These are summarized as

101–500: Statistically Robust or Tentative candidate LESS SMG multiwavelength counterparts from Biggs et al. (2011); see also Wardlow et al. (2011) but which were later shown by ALMA observations to be incorrect IDs (Hodge et al. 2013).

500–700: Robust or tentative IDs for LESS sources with signal-to-noise of $\text{SNR} = 2.7\text{--}3.7\sigma$ in the original LESS map. These IDs for “faint SMGs” are derived using 1.4 GHz radio emission (Biggs et al. 2011) but have not yet been confirmed (or ruled out) by ALMA.

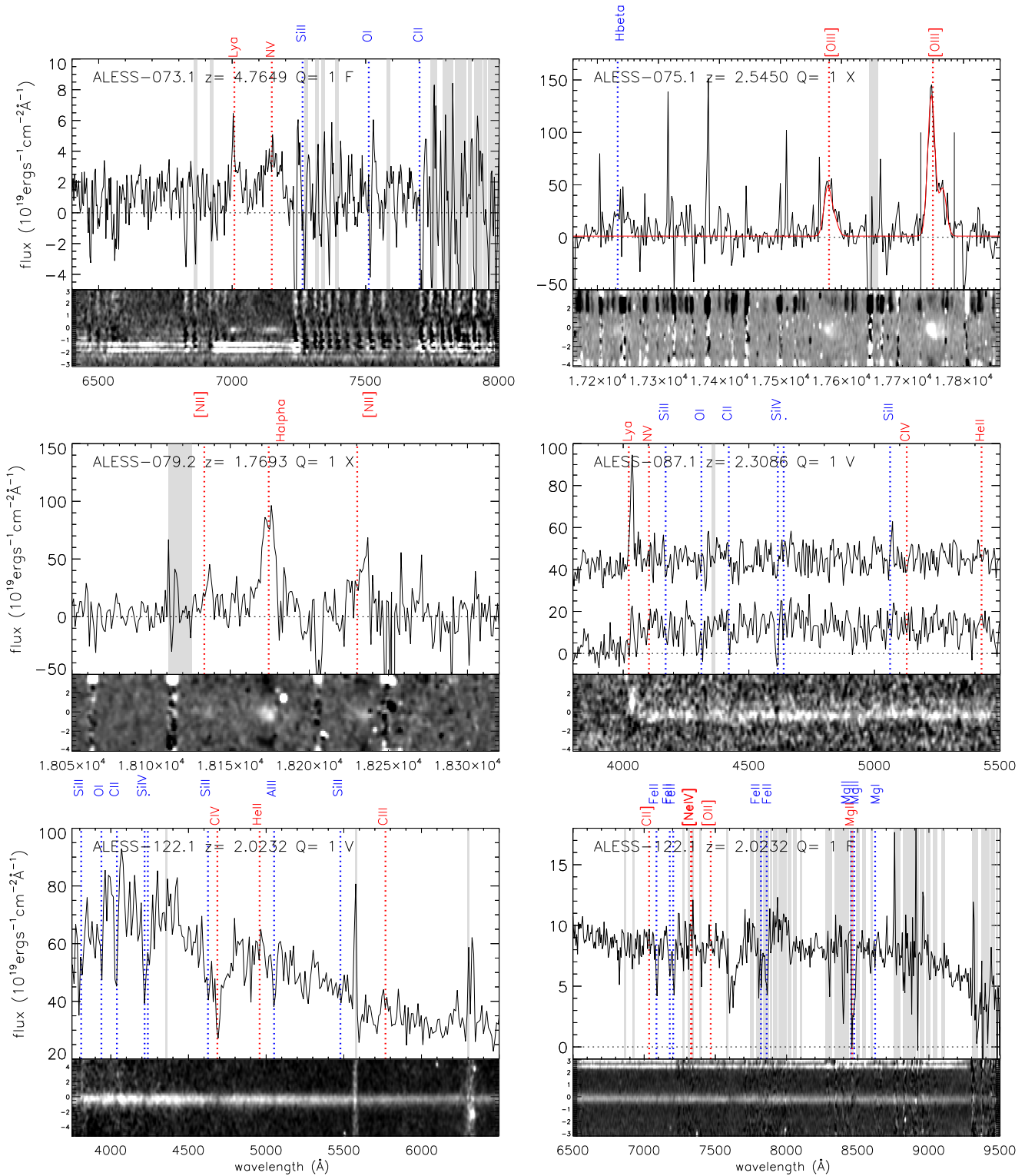


Figure 14. Some of the most notable spectra of SMGs in the sample, featuring evidence of winds, AGN activity, and multiple components. The sky subtraction is poor in some of the spectra and is a particular problem in the near-infrared and in the FORS2 spectrum of ALESS 073.1. The main sky lines have been highlighted in gray.

700–1000: Galaxies in the LESS submillimeter error circles, which have photometric redshifts that are consistent with the ALESS photometric redshifts (Wardlow et al. 2011).

1000–3000: 24 + 70 μ m selected galaxies from the *Spitzer* FIDEL survey without pre-existing spectroscopic redshifts (Magnelli et al. 2009).

4000–4300: *Chandra* X-ray sources from the 2 Ms or 4 Ms surveys (e.g., Lehmer et al. 2005; Luo et al. 2008).

5000–6000: Galaxies from the *Herschel*/SPIRE images, which peak at 350 μ m (and which have been identified and deblended using the 24 μ m positions as priors; Roseboom et al. 2010). Individual redshifts for these sources will be

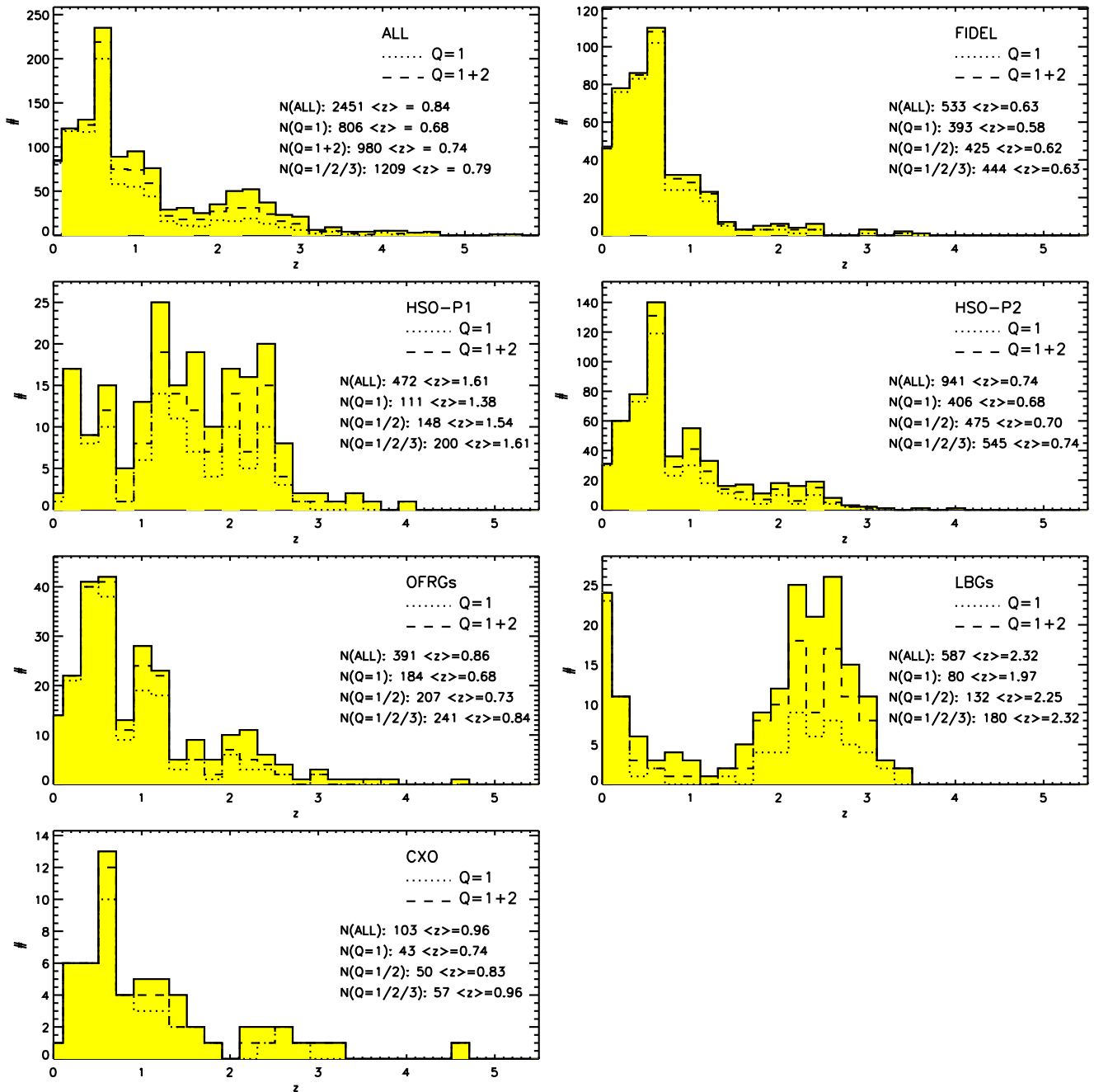


Figure 15. Spectroscopic redshift distributions for the various galaxy population targeted during the spectroscopic campaign. In each panel, we show the redshift distribution for all galaxies, but also show the histograms for the best-quality ($Q = 1$) spectra, and those with $Q = 1$ and 2. The number of galaxies with spectroscopic redshifts (and the median redshift) are also given in the panels. Top left: redshift distribution for ALL galaxies targeted; top right: redshift distribution for 24 μm selected galaxies from the FIDEL survey; middle left: redshift distribution for optically faint radio galaxies (OFRGs); middle right: redshift distribution for the LBGs, BX/BMs, and Ly α emitters; bottom left: redshift distribution for *Chandra* X-ray sources.

published in S. Oliver et al. (2017, in preparation), though we include the redshift distribution in Figure 15.

6000–9800: Galaxies from the *Herschel*/SPIRE images, which peak at 250 μm or 350 μm (and which have been identified and deblended using the 24 μm positions as priors; Roseboom et al. 2010. Individual redshifts for these sources will be published in S. Oliver et al. (2017, in preparation), though we include the redshift distribution in Figure 15.

50000–51000: Optically faint radio galaxies from the JVLA 1.4 GHz survey of this field. These radio sources are typically brighter than $>20 \mu\text{Jy}$ at 1.4 GHz but have optical magnitudes fainter than $I_{\text{AB}} = 22$.

70000–72000: Optically (color) selected galaxies. These comprise a mix of $z \sim 2$ Ly α emitting galaxies, BM/BX galaxies, and Lyman break galaxies at $1.5 < z < 3.5$.

80000–89999: Galaxies that were not in any of the other prior catalogs but that could still be placed on the masks.

90000–90200: *B*- or *V*-band drop-out galaxies (i.e., candidate $z \gtrsim 2.5$ or $z \gtrsim 3.5$ galaxies).

Any source that is labelled with a “*b*” suffix denotes a secondary galaxy that happened to lie on the slit, but is not the primary target.

We also note that the catalogs are not unique (a galaxy could be an ALMA source that is also in the FIDEL 24 μm catalog, a

radio catalog, a BX/BM, and also a *Chandra* X-ray source). In those instances, the object will only appear once in the table, but under the ID from which it was selected for slit placement (i.e., there are no R.A./decl. repeats). As in Table 2, the instrument IDs are denoted by F = VLT/FORS2, V = VLT/VIMOS, X = VLT/XSHOOTER, M = Keck/MOSFIRE, D = Keck /, DEIMOS, and G = Gemini/GNIRS. The quality flag (Q) for the spectroscopic redshifts is $Q = 1$ for secure redshifts; $Q = 2$ for redshifts measured from only one or two strong lines; $Q = 3$ for tentative redshifts measured based on one or two very faint features; $Q = 4$ for those sources that were targeted but no redshift could be determined. The redshift distribution for each of these sub-samples is shown in Figure 15.

References

- Alexander, D. M., Brandt, W. N., Smail, I., et al. 2008, *AJ*, 135, 1968
- Alexander, D. M., Swinbank, A. M., Smail, I., McDermid, R., & Nesvadba, N. P. H. 2010, *MNRAS*, 402, 2211
- Aravena, M., Decarli, R., Walter, F., et al. 2016, *ApJ*, 833, 68
- Balestra, I., Mainieri, V., Popesso, P., et al. 2010, *A&A*, 512, A12
- Barger, A. J., Wang, W.-H., Cowie, L. L., et al. 2012, *ApJ*, 761, 89
- Baugh, C. M., Lacey, C. G., Frenk, C. S., et al. 2005, *MNRAS*, 356, 1191
- B  thermin, M., De Breuck, C., Sargent, M., & Daddi, E. 2015, *A&A*, 576, L9
- Biggs, A. D., Ivison, R. J., Ibar, E., et al. 2011, *MNRAS*, 413, 2314
- Blain, A. W., Chapman, S. C., Smail, I., & Ivison, R. 2004, *ApJ*, 611, 725
- Bonzini, M., Mainieri, V., Padovani, P., et al. 2012, *ApJS*, 203, 15
- Bothwell, M. S., Smail, I., Chapman, S. C., et al. 2013, *MNRAS*, 429, 3047
- Boutsia, K., Leibundgut, B., Trevese, D., & Vagnetti, F. 2009, *A&A*, 497, 81
- Bruzual, G., & Charlot, S. 2003, *MNRAS*, 344, 1000
- Bunker, A. J., Stanway, E. R., Ellis, R. S., McMahon, R. G., & McCarthy, P. J. 2003, *MNRAS*, 342, L47
- Calzetti, D., Armus, L., Bohlin, R. C., et al. 2000, *ApJ*, 533, 682
- Capak, P. L., Riechers, D., Scoville, N. Z., et al. 2011, *Natur*, 470, 233
- Casey, C. M., Berta, S., B  thermin, M., et al. 2012, *ApJ*, 761, 140
- Casey, C. M., Chapman, S. C., Smail, I., et al. 2011, *MNRAS*, 411, 2739
- Casey, C. M., Narayanan, D., & Cooray, A. 2014, *PhR*, 541, 45
- Chabrier, G. 2003, *PASP*, 115, 763
- Chapman, S. C., Blain, A., Ibata, R., et al. 2009, *ApJ*, 691, 560
- Chapman, S. C., Blain, A. W., Smail, I., & Ivison, R. J. 2005, *ApJ*, 622, 772
- Chapman, S. C., Richards, E. A., Lewis, G. F., Wilson, G., & Barger, A. J. 2001, *ApJL*, 548, L147
- Chen, C.-C., Smail, I., Ivison, R. J., et al. 2016, *ApJ*, 820, 82
- Chen, C.-C., Smail, I., Swinbank, A. M., et al. 2015, *ApJ*, 799, 194
- Colless, M., Peterson, B. A., Jackson, C., et al. 2003, arXiv:0306581
- Cooper, M. C., Newman, J. A., Davis, M., Finkbeiner, D. P., & Gerke, B. F. 2012, spec2d: DEEP2 DEIMOS Spectral Pipeline, Astrophysics Source Code Library, ascl:1203.003
- Coppin, K. E. K., Chapman, S. C., Smail, I., et al. 2010, *MNRAS*, 407, L103
- Coppin, K. E. K., Danielson, A. L. R., Geach, J. E., et al. 2012, *MNRAS*, 427, 520
- Coppin, K. E. K., Smail, I., Alexander, D. M., et al. 2009, *MNRAS*, 395, 1905
- Cristiani, S., Appenzeller, I., Arnouts, S., et al. 2000, *A&A*, 359, 489
- Croom, S. M., Shanks, T., Boyle, B. J., et al. 2001, *MNRAS*, 325, 483
- da Cunha, E., Charlot, S., & Elbaz, D. 2008, *MNRAS*, 388, 1595
- da Cunha, E., Walter, F., Smail, I. R., et al. 2015, *ApJ*, 806, 110
- Daddi, E., Dannerbauer, H., Krips, M., et al. 2009, *ApJL*, 695, L176
- Dav  , R., Finlator, K., Oppenheimer, B. D., et al. 2010, *MNRAS*, 404, 1355
- De Breuck, C., Williams, R. J., Swinbank, M., et al. 2014, *A&A*, 565, A59
- Decarli, R., Walter, F., Carilli, C., et al. 2014, *ApJ*, 782, 78
- Dickinson, M., Stern, D., Giavalisco, M., et al. 2004, *ApJL*, 600, L99
- Doherty, M., Bunker, A. J., Ellis, R. S., & McCarthy, P. J. 2005, *MNRAS*, 361, 525
- Dunlop, J. S., McLure, R. J., Biggs, A. D., et al. 2017, *MNRAS*, 466, 861
- Efstathiou, A., & Rowan-Robinson, M. 2003, *MNRAS*, 343, 322
- Erb, D. K., Steidel, C. C., Shapley, A. E., et al. 2006, *ApJ*, 647, 128
- Genzel, R., Baker, A. J., Tacconi, L. J., et al. 2003, *ApJ*, 584, 633
- Georgantopoulos, I., Comastri, A., Vignali, C., et al. 2013, *A&A*, 555, A43
- Hainline, L. J., Blain, A. W., Smail, I., et al. 2009, *ApJ*, 699, 1610
- Hainline, L. J., Blain, A. W., Smail, I., et al. 2011, *ApJ*, 740, 96
- Harrison, C. M., Alexander, D. M., Swinbank, A. M., et al. 2012, *MNRAS*, 426, 1073
- Hayward, C. C., Kere  , D., Jonsson, P., et al. 2011, *ApJ*, 743, 159
- Hickox, R. C., Wardlow, J. L., Smail, I., et al. 2012, *MNRAS*, 421, 284
- Hodge, J. A., Karim, A., Smail, I., et al. 2013, *ApJ*, 768, 91
- Hodge, J. A., Swinbank, A. M., Simpson, J. M., et al. 2016, *ApJ*, 833, 103
- Huynh, M. T., Emonts, B. H. C., Kimball, A. E., et al. 2017, *MNRAS*, 467, 1222
- Huynh, M. T., Norris, R. P., Coppin, K. E. K., et al. 2013, *MNRAS*, 431, L88
- Ikarashi, S., Ivison, R. J., Caputi, K. I., et al. 2015, *ApJ*, 810, 133
- Ivison, R. J., Greve, T. R., Dunlop, J. S., et al. 2007, *MNRAS*, 380, 199
- Ivison, R. J., Smail, I., Dunlop, J. S., et al. 2005, *MNRAS*, 364, 1025
- Ivison, R. J., Swinbank, A. M., Smail, I., et al. 2013, *ApJ*, 772, 137
- Iwasawa, K., Gilli, R., Vignali, C., et al. 2012, *A&A*, 546, A84
- Karim, A., Swinbank, A. M., Hodge, J. A., et al. 2013, *MNRAS*, 432, 2
- Kelson, D. D. 2003, *PASP*, 115, 688
- Kennicutt, R. C. 1998, *ARA&A*, 36, 189
- Kriek, M., van Dokkum, P. G., Franx, M., et al. 2008, *ApJ*, 677, 219
- Kurk, J., Cimatti, A., Daddi, E., et al. 2013, *A&A*, 549, A63
- Lacey, C. G., Baugh, C. M., Frenk, C. S., et al. 2015, *MNRAS*, 462, 3854
- Le F  vre, O., Cassata, P., Cucciati, O., et al. 2013, *A&A*, 559, A14
- Le F  vre, O., Vettolani, G., Garilli, B., et al. 2005, *A&A*, 439, 845
- Lehmer, B. D., Brandt, W. N., Alexander, D. M., et al. 2005, *ApJS*, 161, 21
- Leitherer, C., & Heckman, T. M. 1995, *ApJS*, 96, 9
- Lilly, S. J., Eales, S. A., Gear, W. K. P., et al. 1999, *ApJ*, 518, 641
- Luo, B., Bauer, F. E., Brandt, W. N., et al. 2008, *ApJS*, 179, 19
- Luo, B., Brandt, W. N., Xue, Y. Q., et al. 2011, *ApJ*, 740, 37
- Lutz, D., Poglitsch, A., Altieri, B., et al. 2011, *A&A*, 532, A90
- Magnelli, B., Elbaz, D., Chary, R. R., et al. 2009, *A&A*, 496, 57
- Magnelli, B., Lutz, D., Santini, P., et al. 2012, *A&A*, 539, A155
- Mao, M. Y., Sharp, R., Norris, R. P., et al. 2012, *MNRAS*, 426, 3334
- Martin, C. L., Shapley, A. E., Coil, A. L., et al. 2012, *ApJ*, 760, 127
- Mignoli, M., Cimatti, A., Zamorani, G., et al. 2005, *A&A*, 437, 883
- Narayanan, D., Cox, T. J., Hayward, C. C., Younger, J. D., & Hernquist, L. 2009, *MNRAS*, 400, 1919
- Newman, J. A., Cooper, M. C., Davis, M., et al. 2013, *ApJS*, 208, 5
- Oliver, S. J., Bock, J., Altieri, B., et al. 2012, *MNRAS*, 424, 1614
- Pettini, M., Rix, S. A., Steidel, C. C., et al. 2002, *ApJ*, 569, 742
- Popesso, P., Dickinson, M., Nonino, M., et al. 2009, *A&A*, 494, 443
- Ravikumar, C. D., Puech, M., Flores, H., et al. 2007, *A&A*, 465, 1099
- Roseboom, I. G., Oliver, S. J., Kunz, M., et al. 2010, *MNRAS*, 409, 48
- Rousselot, P., Lidman, C., Cuby, J.-G., Moreels, G., & Monnet, G. 2000, *A&A*, 354, 1134
- Serjeant, S., Farrah, D., Geach, J., et al. 2003, *MNRAS*, 346, L51
- Shapley, A. E. 2011, *ARA&A*, 49, 525
- Shapley, A. E., Steidel, C. C., Pettini, M., & Adelberger, K. L. 2003, *ApJ*, 588, 65
- Silverman, J. D., Mainieri, V., Salvato, M., et al. 2010, *ApJS*, 191, 124
- Simpson, J. M., Smail, I., Swinbank, A. M., et al. 2015a, *ApJ*, 799, 81
- Simpson, J. M., Smail, I., Swinbank, A. M., et al. 2015b, *ApJ*, 807, 128
- Simpson, J. M., Swinbank, A. M., Smail, I., et al. 2014, *ApJ*, 788, 125
- Smail, I., Chapman, S. C., Blain, A. W., & Ivison, R. J. 2004, *ApJ*, 616, 71
- Smolcic, V., Miettinen, O., Tomicic, N., et al. 2017, *A&A*, 597, 4
- Spergel, D. N., Verde, L., Peiris, H. V., et al. 2003, *ApJS*, 148, 175
- Stanway, E. R., Bunker, A. J., McMahon, R. G., et al. 2004a, *ApJ*, 607, 704
- Stanway, E. R., Glazebrook, K., Bunker, A. J., et al. 2004b, *ApJL*, 604, L13
- Steidel, C. C., Erb, D. K., Shapley, A. E., et al. 2010, *ApJ*, 717, 289
- Strolger, L.-G., Riess, A. G., Dahlen, T., et al. 2004, *ApJ*, 613, 200
- Swinbank, A. M., Karim, A., Smail, I., et al. 2012, *MNRAS*, 427, 1066
- Swinbank, A. M., Lacey, C. G., Smail, I., et al. 2008, *MNRAS*, 391, 420
- Swinbank, A. M., Simpson, J. M., Smail, I., et al. 2014, *MNRAS*, 438, 1267
- Szokoly, G. P., Bergeron, J., Hasinger, G., et al. 2004, *ApJS*, 155, 271
- Tacconi, L. J., Genzel, R., Smail, I., et al. 2008, *ApJ*, 680, 246
- Taylor, E. N., Franx, M., van Dokkum, P. G., et al. 2009, *ApJS*, 183, 295
- Toft, S., Smolcic, V., Magnelli, B., et al. 2014, *ApJ*, 782, 68
- Treister, E., Virani, S., Gawiser, E., et al. 2009, *ApJ*, 693, 1713
- Valiante, E., Lutz, D., Sturm, E., et al. 2007, *ApJ*, 660, 1060
- van der Wel, A., Franx, M., van Dokkum, P. G., & Rix, H.-W. 2004, *ApJL*, 601, L5
- Vanzella, E., Cristiani, S., Dickinson, M., et al. 2008, *A&A*, 478, 83
- Walter, F., Decarli, R., Aravena, M., et al. 2016, *ApJ*, 833, 67
- Walter, F., Decarli, R., Carilli, C., et al. 2012, *Natur*, 486, 233
- Wang, S. X., Brandt, W. N., Luo, B., et al. 2013, *ApJ*, 778, 179
- Wardlow, J. L., Smail, I., Coppin, K. E. K., et al. 2011, *MNRAS*, 415, 1479
- Weib, A., De Breuck, C., Marrone, D. P., et al. 2013, *ApJ*, 767, 88
- Weib, A., Kovacs, A., Coppin, K., et al. 2009, *ApJ*, 707, 1201
- Wilkinson, A., Almaini, O., Chen, C.-C., et al. 2017, *MNRAS*, 464, 1380
- Williams, R. J., Maiolino, R., Santini, P., et al. 2014, *MNRAS*, 443, 3780
- Wuyts, S., van Dokkum, P. G., Franx, M., et al. 2009, *ApJ*, 706, 885
- Xia, L., Malhotra, S., Rhoads, J., et al. 2011, *AJ*, 141, 64